

Theory and simulations of two-dimensional vortex motion driven by a background vorticity gradient

David A. Schecter^{a)} and Daniel H. E. Dubin

Physics Department, University of California at San Diego, La Jolla, California 92093

(Received 19 January 2000; accepted 5 February 2001)

This paper examines two-dimensional vortex motion in a shear-flow with nonuniform vorticity. Typically, a vortex travels to an extremum in the background vorticity distribution. In general, the rate of this migration increases with the magnitude of the background vorticity gradient; however, a retrograde vortex, which rotates against the local shear, moves *orders of magnitude* faster than a prograde vortex of equal strength. Retrograde and prograde vortices travel at different speeds because they perturb the background vorticity differently. Linearized equations accurately describe the background vorticity perturbation that is created by a weak retrograde vortex, whereas nonlinear effects dominate for a prograde vortex of any strength. An analytic theory is developed for the velocity of a retrograde vortex, based on the linearized equations. The velocity of a prograde vortex is obtained by a simple “mix-and-move” estimate, which takes into account the nonlinear trapping of fluid around the vortex. Both velocity predictions are verified by vortex-in-cell simulations. If the ratio of background shear to background vorticity gradient exceeds a critical level, there is no vortex motion up or down the background vorticity gradient. Estimates of the critical shear are obtained for both prograde and retrograde vortices. These estimates compare favorably to vortex-in-cell simulations. © 2001 American Institute of Physics. [DOI: 10.1063/1.1359763]

I. INTRODUCTION

Two-dimensional (2D) shear-flows, from laboratory to atmospheric scales, typically contain long-lived vortices. Such vortices are carried along by the shear-flow, but they can also drift in the transverse direction. This transverse drift is generally toward an extremum in the vorticity distribution of the shear-flow, i.e., a peak or trough in the “background” vorticity.

In this article, we derive simple expressions for the rate at which a vortex drifts transverse to the shear-flow, up or down a background vorticity gradient. These analytic results are found to agree with vortex-in-cell simulations of the 2D Euler equations. We focus on the regime where the vortex is point-like, and the background flow has strong shear. In this regime, we find that the vortex speed increases with the magnitude of the local background vorticity gradient, whereas the vortex speed decreases as the local background shear intensifies. When the shear-flow is reversed, the vortex speed changes by *orders of magnitude*. We also demonstrate that there is a critical level of background shear, above which the transverse vortex motion is suppressed. A brief account of some of these results has been published in a previous letter.¹

One motivation for this article is a recent electron plasma experiment² on the free relaxation of an unstable cylindrical shear-flow. In this experiment, a Kelvin–Helmholtz instability generates multiple vortices within the shear-flow. These vortices then “creep” radially outward, down a background vorticity gradient. The outward radial drift causes the

vortices to lose their intensity, so that they are eventually sheared apart. As a result, the shear-flow becomes axisymmetric. This experiment demonstrates that the rate of axisymmetrization can be controlled by the rate at which vortices move along a background vorticity gradient.

Vortex motion on a background gradient also applies to the problem of hurricane motion; here, the background vorticity gradient includes the north-south variation (β) in planetary vorticity. The prediction of hurricane tracks is a problem of great practical importance, so it is hardly surprising that a considerable body of literature has been devoted to the subject.^{3–12} As mentioned earlier, we focus on the regime where (i) the vortex is point-like, and (ii) the background flow has strong shear. Perhaps because this regime is not of direct application to hurricane motion, the results described in this paper (and the earlier letter¹) have not been discussed previously. Nevertheless, while point-like vortices and strong background shear may be rare in geophysical settings, they are common in non-neutral plasmas^{2,13–15} and may also be found on planets like Jupiter that have intense storms in strong zonal winds.¹⁶

We assume that viscosity and compressibility are negligible; that is, we assume that the flow is governed by the 2D Euler equations:

$$\frac{\partial \zeta}{\partial t} + \vec{v} \cdot \nabla \zeta = 0, \quad (1a)$$

$$\vec{v} = \hat{z} \times \nabla \psi, \quad (1b)$$

$$\nabla^2 \psi = \zeta. \quad (1c)$$

Here, $\vec{v}(\vec{r}, t)$ is the velocity field, $\zeta(\vec{r}, t) \equiv \hat{z} \cdot \nabla \times \vec{v}$ is vorticity and $\psi(\vec{r}, t)$ is a stream function. The variable \vec{r} is a 2D po-

^{a)}Present address: Advanced Study Program, National Center for Atmospheric Research, P.O. Box 3000, Boulder, Colorado 80307.

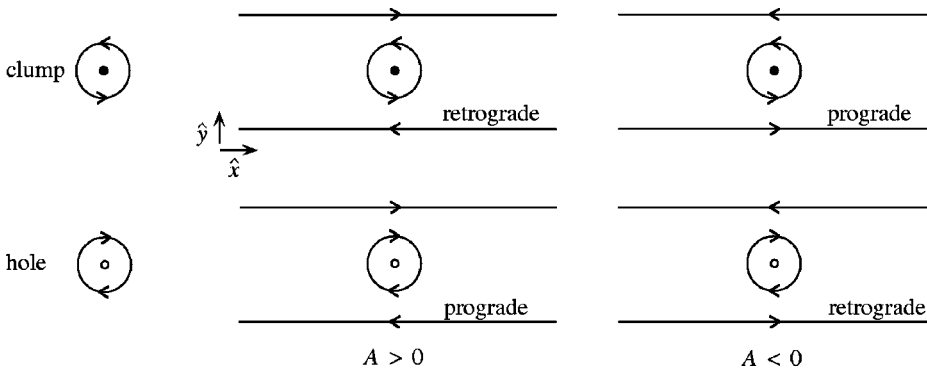


FIG. 1. Both clumps and holes can be retrograde or prograde, depending on the sign of the local shear-rate A .

sition vector ($\hat{z} \cdot \vec{r} = 0$), and t is time. For analysis, the vorticity is decomposed into vortices (v) and background (b): $\zeta = \zeta_b + \sum \zeta_v$.

In order to facilitate discussion, we make the following definitions:

- (i) A vortex is a “clump” if its total circulation Γ_v is positive, whereas a vortex is a “hole” if its total circulation is negative; that is,

$$\begin{aligned} \Gamma_v > 0 & \text{ for clumps,} \\ \Gamma_v < 0 & \text{ for holes,} \end{aligned} \tag{2}$$

where $\Gamma_v \equiv \int d^2r \zeta_v$. This terminology² is motivated by the fact that a clump is a localized excess of vorticity, whereas a hole is a localized deficit of vorticity. In a geophysical context, a clump is a “cyclone” in the northern hemisphere, whereas a hole is an “anticyclone.”¹⁷

- (ii) Suppose that there is a background shear-flow $\vec{v}_b = Ay\hat{x}$ superposed on a vortex at $y=0$, where x and y are Cartesian coordinates. The quantity A (with units of frequency) is called the “local shear-rate” of the flow. Furthermore, the vortex is termed “retrograde” if it rotates against the local shear, whereas it is termed “prograde” if it rotates with the local shear; that is,

$$\begin{aligned} \Gamma_v/A > 0 & \text{ for retrograde vortices,} \\ \Gamma_v/A < 0 & \text{ for prograde vortices.} \end{aligned} \tag{3}$$

The clump/hole status of a vortex determines its *direction* of motion through the background vorticity distribution ζ_b . On the other hand, the *speed* at which a vortex climbs/descends a background vorticity gradient depends on whether it is retrograde or prograde.

As illustrated in Fig. 1, both clumps and holes can be either retrograde or prograde, depending on the sign of the local shear-rate A . In Secs. III–VII, we will focus on the motion of a single small vortex in a cylindrical shear-flow, where the initial background vorticity is positive, axisymmetric and decreases monotonically with radius r . In *this* background, A is positive, making a clump retrograde and a hole prograde.

We now briefly discuss the basic physics of vortex motion driven by a background vorticity gradient. It is well known that clumps ascend a background vorticity gradient,

whereas holes descend the gradient.^{3,18} Figure 2 illustrates this phenomenon for the case of cylindrical geometry, point-like vortices and strong background shear. At $t=0$, a clump (black spot) and a hole (white spot) are placed in a cylindrical shear-flow. The system is evolved with a vortex-in-cell (VIC) simulation that numerically integrates the 2D Euler equations (see Ref. 15 for a description of the VIC simulation). Eventually, the clump is driven to the peak in background vorticity, whereas the hole is driven toward the minimum.

Figure 3 shows the gradient-driven separation of a clump and hole in straight zonal flow. The flow is evolved using a VIC simulation in a periodic box. As before (Fig. 2), the clump migrates to the peak in background vorticity, whereas the hole migrates to the minimum. Thus, clumps and holes tend to opposite extremes in the background vorticity, in both curved and uncurved geometry.

When the boundary conditions have rotational or translational symmetry, the opposite drifts of clumps and holes are easily explained using conservation of angular or linear momentum. Similar arguments have been used to explain the motion of phase-space density clumps and holes in plasma turbulence.¹⁹

We first consider a small clump [Fig. 4(a)] or hole [Fig. 4(b)] in an initially axisymmetric background $\zeta_b(r, \theta, t)$ that decreases slowly with r . Here, (r, θ) is a polar coordinate system, with its origin at the center of the background. In time, background vorticity contours tend to wrap around the vortex, or evolve in such a way that a plateau starts to form in the θ -averaged background vorticity profile. We refer to this process as the local “phase-mixing” of vorticity.

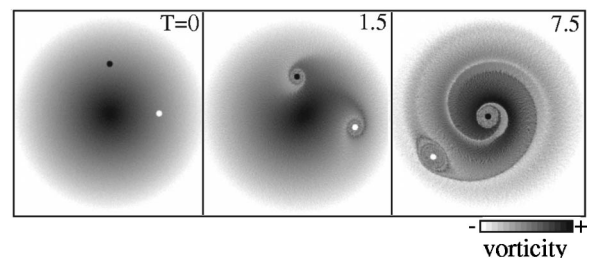


FIG. 2. VIC simulation of the gradient-driven radial separation of a clump (black dot) and hole (white dot) in a cylindrical shear-flow [Eq. (39)]. T is a dimensionless measure of time that is introduced in Sec. II [following Eq. (16)].

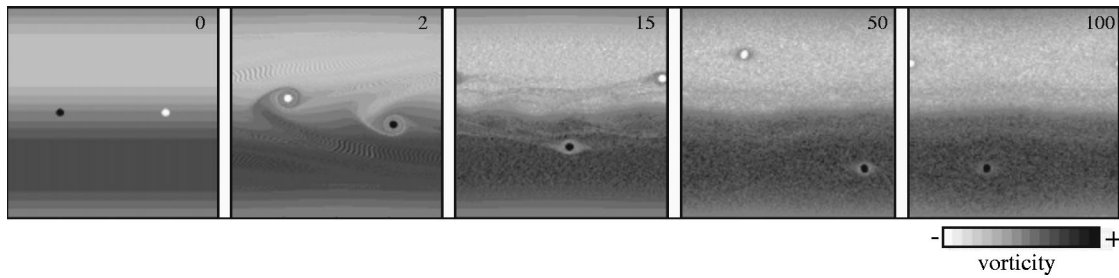


FIG. 3. VIC simulation of the gradient-driven separation of a clump and hole in straight zonal flow. The numbers on each snap-shot indicate time in arbitrary units.

The phase-mixing of background vorticity near the vortex causes the vortex to move. If the fluid is contained by a free-slip cylindrical boundary at $r=R_w$, the motion is constrained by conservation of canonical angular momentum,¹⁷ $P_\theta \equiv \int d^2r r^2 \zeta(r, \theta, t)$. This canonical angular momentum is a convenient simplification of the actual angular momentum per unit length of the fluid, which is defined by the equation $\mathcal{L} \equiv \hat{z} \cdot \int d^2r \vec{r} \times \rho \vec{v} = \frac{1}{2} \rho (\Gamma_{\text{tot}} R_w^2 - P_\theta)$. Here, ρ is the uniform mass density of the fluid, and Γ_{tot} is the total circulation of the flow.

It is convenient to write P_θ in terms of a background contribution and a vortex contribution,

$$P_\theta = \Gamma_b \langle r^2 \rangle_b + \Gamma_v r_v^2. \tag{4}$$

Here $\Gamma_b > 0$ is the total circulation of the background flow, Γ_v is the vortex circulation, r_v is the radial position of the vortex and $\langle r^2 \rangle_b$ denotes the ζ_b -weighted spatial average of r^2 . As shown in Fig. 4, local phase-mixing increases $\langle r^2 \rangle_b$ by flattening the background [since $\zeta'_b(r) < 0$]. To conserve P_θ , the clump ($\Gamma_v > 0$) must decrease r_v and climb the background gradient, whereas the hole ($\Gamma_v < 0$) must increase r_v and descend the gradient, as observed in Fig. 2.

If the fluid is bounded by parallel walls at $y = \pm Y$, the 2D Euler equations conserve P_x , the canonical linear momentum:¹⁷

$$P_x \equiv \int d^2x y \zeta(x, y, t) = \Gamma_b \langle y \rangle_b + \Gamma_v y_v. \tag{5}$$

Here (x, y) is a rectangular coordinate system in the plane of the flow. The motion of a vortex along the y -gradient in ζ_b can be explained by conservation of P_x , just as motion along the radial gradient was explained by conservation of P_θ in cylindrical flow. If $\zeta'_b(y) < 0$, local phase-mixing increases $\langle y \rangle_b$. By conservation of P_x a clump must climb the gradient and decrease y_v , whereas a hole must descend the gradient and increase y_v .

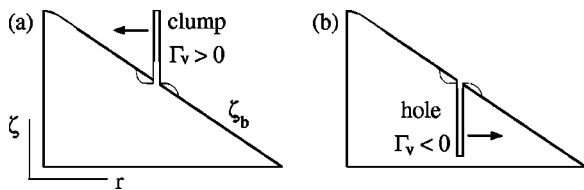


FIG. 4. Local phase-mixing of the background vorticity increases $\langle r^2 \rangle_b$. By conservation of P_θ , clumps and holes react oppositely.

When there is no local vorticity gradient, local phase-mixing does not affect the background vorticity distribution. Therefore, where $\zeta'_b = 0$, there is no local mechanism for the vortex to exchange angular or linear momentum with the background. This suggests that clumps will settle on hills of background vorticity and that holes will settle in troughs, where $\zeta'_b = 0$. This relaxation principle is consistent with Figs. 2 and 3.

We now turn our discussion to the speed of the vortex motion. We will see in Sec. IV that retrograde vortices move toward extrema of ζ_b orders of magnitude faster than prograde vortices of equal strength $|\Gamma_v|$. This is because retrograde and prograde vortices perturb the background vorticity differently. In the case of a weak retrograde vortex, a linear model (Secs. II and III) provides a good approximation for the evolution of the background vorticity perturbation. Using this linear model, we will obtain an analytic expression for the vortex velocity that agrees with vortex-in-cell simulations. On the other hand, a prograde vortex generally creates a nonlinear perturbation to the background vorticity, over the time scale of interest. As a result, the motion of a prograde vortex is better described by a simple ‘‘mix-and-move’’ model, which we will describe in Sec. VI.

A sufficiently large background shear will suppress the gradient-driven motion of both retrograde and prograde vortices. For both cases, we will estimate the critical levels of shear that are required to prevent excursions toward extrema of ζ_b . These estimates compare favorably to vortex-in-cell simulations.

We now give an outline of the main text. In Sec. II, we present a simple linear theory of vortex motion that is driven by a background vorticity gradient (an abbreviated version of this simple theory appears in Ref. 1). In Sec. III, we present a more detailed linear theory for the case of a weak vortex in a cylindrical shear flow. In Sec. IV, we compare the linear theory of Sec. III to a nonlinear VIC simulation. We find that linear theory works well only for retrograde vortices, and fails for prograde vortices. In Sec. V, we discuss why linear theory fails for prograde vortices. In Sec. VI, we obtain a more accurate estimate of the velocity of a prograde vortex in a cylindrical shear-flow, using a simple ‘‘mix-and-move’’ model. In Sec. VII, we show that gradient-driven vortex motion is suppressed when the local shear-rate is sufficiently large. In Sec. VIII, we summarize our results, and discuss some physical systems where they may apply. Many intermediate results are derived in the appendices.

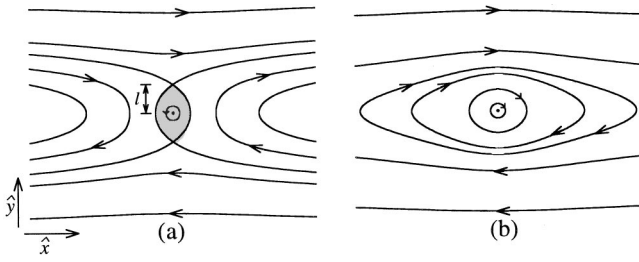


FIG. 5. Initial streamlines near a retrograde vortex (a) and a prograde vortex (b) in a linear shear-flow $\vec{v}_b = Ay\hat{x}$, $A > 0$.

II. SIMPLE CALCULATION OF GRADIENT-DRIVEN DRIFT

In this section, we determine the speed at which a point-vortex in a shear-flow moves up/down a background vorticity gradient, making a few reasonable approximations that reduce the algebra. A more detailed analysis is presented in Sec. III, for the case of a point-vortex in a cylindrical shear-flow.

For simplicity, we suppose that the initial velocity field near the vortex is given approximately by

$$\vec{v}(x, y, t=0) = Ay\hat{x} + \frac{\Gamma_v}{2\pi} \frac{x\hat{y} - y\hat{x}}{x^2 + y^2}. \quad (6)$$

Here, (x, y) is a rectangular coordinate system, centered at the initial vortex position. The first term on right-hand-side of Eq. (6) is the first nonzero term in a Taylor expansion (about $x, y = 0$) of the initial background shear-flow. The second term in Eq. (6) is the vortex velocity field. We also assume that there is an approximately uniform vorticity gradient, $\zeta'_o \hat{y}$, in the region of interest surrounding the vortex.

Figure 5 shows the velocity field that is given by Eq. (6), for the case of a clump (a) and a hole (b). In this figure, $A > 0$, so the clump is retrograde and the hole is prograde. For a retrograde vortex [Fig. 5(a)], there are stagnation points at a distance l above and below the vortex, where

$$l \equiv \sqrt{|\Gamma_v/2\pi A|}. \quad (7)$$

It is evident that the vortex velocity field dominates the background shear-flow at distances less than l from the vortex. For a prograde vortex, there are no stagnation points, and we will see (Secs. IV–VII) that this fact has a profound effect on the evolution of the system.

In time, the vortex creates a perturbation $\delta\zeta_b(x, y, t)$ to the background vorticity, and moves in response. The Euler equation for the evolution of vorticity [Eq. (1a)] can be written as a set of two coupled equations: one for the evolution of $\delta\zeta_b$, and the other for the point-vortex trajectory, $\vec{x}_v(t)$. The equation for $\delta\zeta_b$ near the vortex is given by

$$\frac{\partial \delta\zeta_b}{\partial t} + \left[Ay - \frac{\partial \delta\psi}{\partial y} \right] \cdot \frac{\partial \delta\zeta_b}{\partial x} + \frac{\partial \delta\psi}{\partial x} \cdot \left[\zeta'_o + \frac{\partial \delta\zeta_b}{\partial y} \right] = 0, \quad (8)$$

where $\delta\psi$ is the stream function perturbation. The stream function perturbation satisfies the equation

$$\nabla^2 \delta\psi = \delta\zeta_b + \Gamma_v \delta(\vec{x} - \vec{x}_v), \quad (9)$$

where $\delta(\vec{x} - \vec{x}_v)$ is the two-dimensional Dirac delta-function, centered at the vortex position. The equation for the vortex trajectory is given by

$$\dot{\vec{x}}_v = A y_v \hat{x} + \hat{z} \times \nabla \delta\psi|_{\vec{x}_v}, \quad (10)$$

where $x_v(t)$ and $y_v(t)$ are the vortex coordinates along the x -axis and y -axis, respectively.

If the vortex is sufficiently weak ($\Gamma_v \rightarrow 0$), it is reasonable to neglect terms in Eq. (8) that are second order in $\delta\psi$ and $\delta\zeta_b$. Then, we are left with the linearized Euler equation,

$$\frac{\partial \delta\zeta_b}{\partial t} + Ay \frac{\partial \delta\zeta_b}{\partial x} + \frac{\partial \delta\psi}{\partial x} \zeta'_o = 0. \quad (11)$$

This linearized Euler equation clearly breaks down at distances less than l [Eq. (7)] from the point-vortex, where the vortex velocity field (incorporated in $\delta\psi$) can not be treated as a perturbation to the background shear-flow. The time scale for the linearized Euler equation to remain valid is addressed in Sec. V.

We focus our present attention on the initial evolution of $\delta\zeta_b$. During this ‘‘fast time scale,’’ the vortex is approximately stationary; that is, $\vec{x}_v \approx 0$. We also assume that, in the background, the vortex contribution to $\delta\psi$ [Eq. (9)] dominates the contribution from $\delta\zeta_b$. This implies that, in the background, $\delta\psi \approx (4\pi)^{-1} \Gamma_v \ln(x^2 + y^2)$. Using this approximation, Eq. (11) reduces to

$$\left[\frac{\partial}{\partial t} + Ay \frac{\partial}{\partial x} \right] \cdot \delta\zeta_b + \zeta'_o \frac{\Gamma_v}{2\pi} \frac{x}{x^2 + y^2} = 0. \quad (12)$$

Equation (12) can be solved by the method of characteristics, yielding

$$\delta\zeta_b = \frac{-\Gamma_v}{4\pi} \frac{\zeta'_o}{Ay} \ln \left[\frac{x^2 + y^2}{(x - Ayt)^2 + y^2} \right]. \quad (13)$$

The transverse velocity \dot{y}_v of the vortex is given by the y -component of Eq. (10), which has the following integral solution:

$$\begin{aligned} \dot{y}_v &= \frac{\partial \delta\psi}{\partial x} \Big|_{\vec{x}_v} \\ &= \frac{1}{2\pi} \int_{-\infty}^{\infty} \int_{-\infty}^{\infty} dy dx \frac{x_v - x}{(x_v - x)^2 + (y_v - y)^2} \delta\zeta_b(x, y, t). \end{aligned} \quad (14)$$

Over the fast time scale, the vortex remains close to the origin; so, we let $\vec{x}_v \approx 0$ in Eq. (14). If in addition we substitute the linear result [Eq. (13)] for $\delta\zeta_b$ into Eq. (14), we obtain

$$\dot{y}_v = \frac{\Gamma_v}{4\pi^2} \frac{\zeta'_o}{A} \int_l^L \frac{dy}{y} \int_{-\infty}^{+\infty} du \frac{u}{u^2 + 1} \ln \left[\frac{u^2 + 1}{(u - At)^2 + 1} \right], \quad (15)$$

where $u \equiv x/y$. A small scale (l) and a large scale (L) cut-off are introduced in the y -integral to keep \dot{y}_v finite. The small scale cut-off l is given by Eq. (7): at distances closer to the origin (the vortex), the linear-result [Eq. (13)] for $\delta\zeta_b$ is

invalid. The large scale cut-off L is ambiguous, without further specification of the background shear-flow. Presumably, L is the distance from the vortex where our initial approximations of the background shear-flow become inaccurate. If the background velocity field is curved, as opposed to $\vec{v}_b = Ay\hat{x}$, then L is likely the radius of curvature at the vortex position. If the shear-flow is straight, then L is likely the length scale for variations in ζ'_o . In any case, we have assumed that the vortex is sufficiently weak, so that l is much less than L . We have also assumed that the contributions from $\delta\zeta_b$ at short ($\leq l$) and long ($\geq L$) distances from the vortex have negligible contributions to \dot{y}_v .

The integrals in Eq. (15) yield

$$\begin{aligned} \dot{y}_v &= \frac{\Gamma_v}{2\pi} \frac{\zeta'_o}{|A|} \ln(L/l) \cdot \tan^{-1}(T/2) \\ &= \pm \zeta'_o l^2 \ln(L/l) \cdot \tan^{-1}(T/2), \end{aligned} \tag{16}$$

where $T \equiv |A|t$ and $+/-$ is for clumps/holes. The u -integral, which gives the time dependence, is evaluated in Appendix A. For $T \gg 1$, the inverse-tangent is approximately $\pi/2$ and \dot{y}_v is approximately constant.

Over a slow time scale, the vortex moves a distance of order L , and the stationary vortex approximation that is used for Eqs. (12)–(16) is invalid. We propose that over this slow time scale ($T \gg 1$), the transverse velocity \dot{y}_v is given by the time-asymptotic limit of Eq. (16), with ζ'_o and l changing as the vortex moves. This model of the slow vortex motion is reasonable only if the vortex is sufficiently weak, so that the time for the vortex to move a distance l (the small scale cut-off) is much greater than $T = 1$ ($t = |A|^{-1}$).

We note that a similar argument is made in the text-book theory of a charged particle that is decelerated by Cerenkov radiation.²⁰ In this theory, the asymptotic force on a charged particle, emitting waves in a plasma, is calculated keeping the particle fixed on its unperturbed trajectory. This asymptotic force is then assumed to change parametrically with slow changes in the particle’s position and velocity.

Equation (16) gives a reasonable scaling for the vortex speed: \dot{y}_v increases with Γ_v and ζ'_o , whereas it decreases as the local shear-rate A intensifies. However, the validity of Eq. (16) rests on the accuracy of Eq. (12), which neglects (among other things) curvature in the background shear-flow, and the contribution to $\delta\psi$ from $\delta\zeta_b$. In the next section, we will calculate the transverse velocity of a vortex in a cylindrical shear-flow, keeping these effects. This calculation reproduces Eq. (16) in the time asymptotic limit. It also provides a precise argument for the logarithm, so that we can compare vortex-in-cell simulations to an analytic theory that has no free parameters.

III. LINEAR THEORY OF GRADIENT-DRIVEN VORTEX MOTION IN A CYLINDRICAL SHEAR-FLOW

We now calculate the radial velocity of a point-vortex in a cylindrical shear-flow. For this case, it is convenient to use a polar (r, θ) coordinate system which has its origin at the center of the background. We denote the initial vorticity profile and angular rotation frequency of the background shear-

flow by $\zeta_o(r)$ and $\Omega_o(r)$, respectively. In addition, we denote the radial and angular positions of the vortex by $r_v(t)$ and $\theta_v(t)$.

We restrict our attention to weak vortices. To make this statement quantitative, we introduce the dimensionless parameter

$$l/r_v = \frac{1}{r_v} \sqrt{\left| \frac{\Gamma_v}{2\pi r_v \Omega'_o(r_v)} \right|}. \tag{17}$$

Here, l is the “trapping length” that is defined by Eq. (7), with $A \equiv -r_v \Omega'_o(r_v)$. A vortex is “weak” if $l/r_v \ll 1$. The initial streamlines near ($|\vec{r} - \vec{r}_v| \ll r_v$) a weak vortex in a cylindrical shear flow closely resemble the streamlines in Fig. 5, provided that the flow is viewed in a rotating frame, where the vortex is initially at rest. To convert Fig. 5 to cylindrical geometry, simply let $\hat{y} \rightarrow \hat{r}$ and $\hat{x} \rightarrow -\hat{\theta}$, where \hat{r} and $\hat{\theta}$ are the radial and azimuthal unit vectors (at the vortex position).

In time, the vortex creates a perturbation $\delta\zeta_b$ to the background vorticity distribution. This perturbation is defined by the equation

$$\zeta_b(r, \theta, t) = \zeta_o(r) + \delta\zeta_b(r, \theta, t). \tag{18}$$

The stream function can also be written as that of the unperturbed shear-flow plus a perturbation; i.e.,

$$\psi(r, \theta, t) = - \int_r^{R_w} dr' r' \Omega_o(r') + \delta\psi(r, \theta, t). \tag{19}$$

The perturbation $\delta\psi$ consists of a background contribution and a vortex contribution, that is,

$$\nabla^2 \delta\psi = \delta\zeta_b + \Gamma_v \frac{\delta(r - r_v) \delta(\theta - \theta_v)}{r_v}. \tag{20}$$

The boundary condition is $\delta\psi = 0$ at the wall radius R_w .

As in Sec. II, we rewrite the Euler equation for the evolution of vorticity [Eq. (1a)] as a set of two coupled equations: one for the evolution of $\delta\zeta_b$, and the other for the point-vortex trajectory, $\vec{r}_v(t) = r_v(t)\hat{r}(t)$. The equation for the evolution of $\delta\zeta_b$ is

$$\begin{aligned} \frac{\partial \delta\zeta_b}{\partial t} + \left[\Omega_o(r) + \frac{1}{r} \frac{\partial \delta\psi}{\partial r} \right] \cdot \frac{\partial \delta\zeta_b}{\partial \theta} - \frac{1}{r} \frac{\partial \delta\psi}{\partial \theta} \\ \cdot \left[\zeta'_o(r) + \frac{\partial \delta\zeta_b}{\partial r} \right] = 0. \end{aligned} \tag{21}$$

The equation for the vortex trajectory is

$$\dot{\vec{r}}_v = r_v \Omega_o(r_v) \hat{\theta} + \hat{z} \times \nabla \delta\psi|_{\vec{r}_v}. \tag{22}$$

Equations (21) and (22) are coupled, since $\delta\psi$ [Eq. (20)] depends on both $\delta\zeta_b$ and \vec{r}_v .

Because the vortex is weak ($l/r_v \ll 1$), it is reasonable to neglect terms in Eq. (21) that are second order in $\delta\psi$ and $\delta\zeta_b$. We are then left with the linearized Euler equation,

$$\frac{\partial \delta\zeta_b}{\partial t} + \Omega_o(r) \frac{\partial \delta\zeta_b}{\partial \theta} - \frac{1}{r} \frac{\partial \delta\psi}{\partial \theta} \zeta'_o(r) = 0. \tag{23}$$

We note that Eq. (23) incorporates curvature in the background shear-flow, which was neglected in the linear theory

of Sec. II. In addition, Eq. (23) keeps the background contribution to $\delta\psi$ [via Eq. (20)], which was also ignored (eventually) in Sec. II.

It is convenient to expand the perturbation, using a Fourier series in the polar angle θ :

$$\begin{pmatrix} \delta\psi \\ \delta\zeta_b \end{pmatrix} = \sum_{m=-\infty}^{\infty} e^{im\theta} \begin{pmatrix} \Psi^{(m)}(r,t) \\ Z^{(m)}(r,t) \end{pmatrix}. \quad (24)$$

Substituting Eqs. (24) into Eq. (23), it is found that each Fourier coefficient of the vorticity perturbation evolves independently, according to

$$\left[\frac{\partial}{\partial t} + im\Omega_o(r) \right] \cdot Z = im \frac{\zeta'_o(r)}{r} \Psi. \quad (25)$$

Here, we have suppressed the superscript “(m)” on Z and Ψ . This will be standard, unless it would cause ambiguity.

According to Eq. (22), the radial velocity of the vortex is $\dot{r}_v = -(1/r_v)(\partial\delta\psi/\partial\theta)|_{\vec{r}_v}$, which can be written

$$\dot{r}_v = \frac{2}{r_v} \sum_{m=1}^{\infty} m \cdot \text{Im}[\Psi^{(m)}(r_v, t) e^{im\theta_v}]. \quad (26)$$

Here, Im stands for the imaginary part of the quantity in square brackets. We assume that the angular velocity of the vortex $\dot{\theta}_v$ is dominated by the unperturbed background rotation. So, we use the following approximation,

$$\dot{\theta}_v = \Omega_o(r_v). \quad (27)$$

Equation (27) is justified upon comparison to numerical simulations of the exact vortex motion (e.g., Fig. 7 in Sec. IV).

The value of \dot{r}_v is now calculated using an *unperturbed orbit approximation*. In this approximation, the background perturbation is evolved with the vortex moving along an unperturbed circular orbit, and \dot{r}_v is taken to be the radial velocity perturbation that develops at \vec{r}_v . Based on Sec. II, we expect that \dot{r}_v rapidly ($t \sim |A|^{-1} = |r_v \Omega'_o(r_v)|^{-1}$) asymptotes to a finite value. We will show [Eq. (38)] that this asymptotic speed is a function of the vortex strength l and the local background vorticity gradient $\zeta'_o(r_v)$. We propose that over a slow time scale ($t \gg |A|^{-1}$), \dot{r}_v is given by this function, with $\zeta'_o(r_v)$ and l changing as the vortex moves through the background.

According to Eq. (26), to calculate \dot{r}_v , we must calculate the Fourier coefficients $\{\Psi^{(m)}\}$ of the stream function. Let $\tilde{Z}(r,s)$ and $\tilde{\Psi}(r,s)$ denote the temporal Laplace transforms of $Z(r,t)$ and $\Psi(r,t)$. Here, s is the Laplace transform variable. From Eq. (25), and the initial condition $Z(r,0)=0$, we have

$$[s + im\Omega_o(r)] \cdot \tilde{Z} = im \frac{\zeta'_o(r)}{r} \tilde{\Psi}. \quad (28)$$

From Eq. (20),

$$\left[\frac{\partial^2}{\partial r^2} + \frac{1}{r} \frac{\partial}{\partial r} - \frac{m^2}{r^2} \right] \cdot \tilde{\Psi} = \tilde{Z} + \frac{\Gamma_v}{2\pi s} \frac{\delta(r-r_v)}{r}. \quad (29)$$

Note that Eq. (29) is written for a frame that rotates with the the orbital frequency of the vortex. In this frame, $\dot{\theta}_v = \Omega_o(r_v) = 0$, and we have set θ_v equal to zero.

Combining Eq. (28) with Eq. (29), we obtain the following equation for $\tilde{\Psi}(r,s)$:

$$\tilde{\Psi}(r,s) \equiv \frac{\Gamma_v}{2\pi s} G(r|r_v, s). \quad (30)$$

Here, G is the Green’s function of a differential operator D_s ,

$$D_s[G(r|r_v, s)] = \frac{\delta(r-r_v)}{r}, \quad (31)$$

and D_s is defined by the equation

$$D_s \equiv \frac{\partial^2}{\partial r^2} + \frac{1}{r} \frac{\partial}{\partial r} - \frac{m^2}{r^2} - \frac{im\zeta'_o(r)}{r[s + im\Omega_o(r)]}. \quad (32)$$

To obtain $\Psi(r,t)$, we must invert the Laplace transform [Eq. (30)]. This yields the following integral expression for $\Psi(r,t)$:

$$\Psi(r,t) = \frac{\Gamma_v}{4\pi^2 i} \int_{\alpha-i\infty}^{\alpha+i\infty} ds \frac{G(r|r_v, s)}{s} e^{st}. \quad (33)$$

The integral in Eq. (33) is along the vertical line $s \equiv \alpha + i\omega$ in the complex plane, where α is positive and $-\infty < \omega < \infty$.

For now, we follow standard procedure, and neglect any poles of $G(r|r_v, s)$ that might exist in the right half of the complex s -plane (including the imaginary axis). We then use the Plemelj formula to obtain the following limit of Eq. (33) as $\alpha \rightarrow 0^+$:

$$\Psi(r,t) = \frac{\Gamma_v}{4\pi^2 i} \left\{ P \int_{-\infty}^{\infty} d\omega \frac{G(r|r_v, 0^+ + i\omega)}{\omega} e^{i\omega t} + i\pi G(r|r_v, 0^+) \right\}. \quad (34)$$

Here, P denotes the “principal part” of the integral, which has a singular integrand at $\omega=0$.

From our simple calculation [Eq. (16)], we found that \dot{r}_v (there \dot{y}_v) rapidly asymptotes to a constant value. We assume that the same is true here, and concern ourselves only with this time-asymptotic limit. In Appendix D, we show that the time-asymptotic limit of the integral in Eq. (34) is $i\pi G(r|r_v, 0^+)$. Therefore,

$$\lim_{t \rightarrow \infty} \text{Im}[\Psi(r,t)] = \frac{\Gamma_v}{2\pi} \text{Im}[G(r|r_v, 0^+)]. \quad (35)$$

Substituting Eq. (35) into Eq. (26), we find that the time-asymptotic value of the radial drift is given by the following equation:

$$\lim_{t \rightarrow \infty} \dot{r}_v = \frac{\Gamma_v}{\pi r_v} \sum_{m=1}^{\sqrt{\bar{e}} r_v / l} m \cdot \text{Im}[G^{(m)}(r_v|r_v, 0^+)] = \pm 2|\Omega'_o(r_v)| l^2 \sum_{m=1}^{\sqrt{\bar{e}} r_v / l} m \cdot \text{Im}[G^{(m)}(r_v|r_v, 0^+)], \quad (36)$$

where $+/-$ is for clumps/holes.

In Eq. (36), we have truncated the series at $m = \sqrt{e}r_v/l$. This value of m is one over the azimuthal width (in radians) of the small trapping region (TR) that surrounds a retrograde vortex [the shaded area in Fig. 5(a)]. Shortly, we will see that the series in Eq. (36) diverges logarithmically as the upper limit of m approaches infinity, so that a large m cut-off is necessary.

The series divergence in Eq. (36) is an artifact of using the linearized vorticity equation [Eq. (23)] to describe the evolution of $\delta\zeta_b$ in the TR. In the TR, the circular vortex flow dominates the background shear-flow, contrary to the assumption that led to Eq. (23). The perturbation in the TR is represented by wave-numbers $m \gtrsim \sqrt{e}r_v/l$; therefore, $m = \sqrt{e}r_v/l$ is the appropriate cut-off.

Of course, neglecting $m > \sqrt{e}r_v/l$ amounts to neglecting the contribution to \dot{r}_v from $\delta\zeta_b$ in the TR. This is physically reasonable as $l/r_v \rightarrow 0$, and the area ($\sim l^2$) of the TR becomes vanishingly small. Although the TR is defined only for a retrograde vortex, we will try the same cut-off for a prograde vortex.

For small m , the Green's function $G(r|r_v, 0^+)$ must (in general) be found numerically, as discussed in Appendix B. However, for large m , the imaginary part of the Green's function can be calculated analytically. From this analytic calculation, we obtain

$$\text{Im}[G(r_v|r_v, 0^+)] \rightarrow \frac{\pi \zeta'_o(r_v)}{4m^2 |\Omega'_o(r_v)|}, \quad m \gg 1. \quad (37)$$

Equation (37) is derived in Appendix B.

Because of Eq. (37), the sum in Eq. (36) diverges logarithmically as the m -number cut-off goes to infinity, i.e., as $l/r_v \rightarrow 0$. Thus, for sufficiently weak vortices, the time asymptotic radial drift is approximately given by

$$\dot{r}_v = \pm \frac{\pi}{2} \zeta'_o(r_v) l^2 \ln(c \cdot r_v/l). \quad (38)$$

Here, $+/-$ is for clumps/holes, and c is determined by the low- m values of the Green's function $G^{(m)}(r_v|r_v, 0^+)$. Note that Eq. (38) is equivalent to the $T \rightarrow \infty$ limit of our back-of-the-envelope calculation, Eq. (16), with $\dot{y}_v \rightarrow \dot{r}_v$ and $L \rightarrow c r_v$.

In practice, we obtain the value of c by setting Eq. (38) equal to a numerical solution of Eq. (36) for any large value of the m -number cut-off, $\sqrt{e}r_v/l$. The resulting equation is easily solved for c . As an example, we consider the radial velocity of a vortex at $r_v = 0.4$, in the background distribution of Eq. (39) (see next section). For this case, we obtain $c = 0.43$. In Fig. 6, we plot the time asymptotic value of \dot{r}_v , given by Eq. (36), versus $\sqrt{e}r_v/l$. Also in this figure, we plot the time asymptotic value of \dot{r}_v that is given by Eq. (38), with $c = 0.43$. Clearly, Eq. (38) is an excellent approximation of \dot{r}_v for all $l/r_v \leq 0.1$. Although c in general depends on r_v , we find that for the vorticity profile of Eq. (39), $c = 0.43$ works for all $r_v \leq 0.7$.

Finally, the linear theory presented in this section neglects poles (in the s -plane) of the Green's function $G(r|r_v, s)$. This amounts to neglecting the excitation by the vortex of discrete modes in the background. In the next sec-

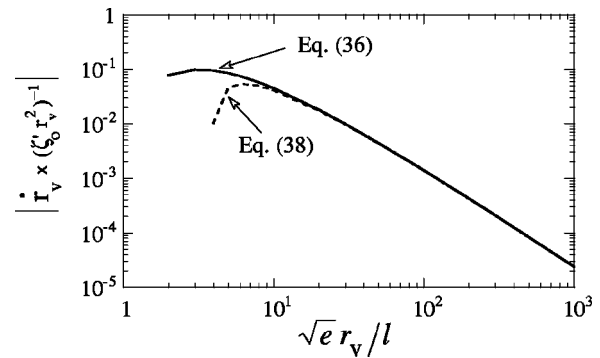


FIG. 6. Comparison of Eq. (36) for \dot{r}_v to the large $\sqrt{e}r_v/l$ approximation, Eq. (38).

tion we will show that neglecting the excitation of discrete modes is acceptable, for a case where the background vorticity varies slowly with r . However, vortex-mode interactions may be important when there are large steps in the radial profile of the background.²¹

IV. THE SUCCESS AND FAILURE OF LINEAR THEORY

We now demonstrate that the linear equations of motion apply only to retrograde vortices, and that nonlinear effects must be kept to explain the slower drift of prograde vortices. We reach this conclusion first by comparing a (nonlinear) VIC simulation²² to a numerical integration of the linearized equations [Eqs. (25)–(27)]. In both simulations, the fluid is bounded by a cylindrical wall of radius R_w , at which there is free slip ($\psi = 0$ at R_w). In the following, frequencies are measured in units of $\zeta_o(0)$, and lengths are measured in units of R_w . Furthermore, the flow is viewed in a rotating frame, where the vortex is initially at rest [$\dot{r}_v(0) = 0$].

In the linear simulation, the vortex position \vec{r}_v and the Fourier coefficients $\{Z^{(m)}\}$ of the background vorticity are evolved forward in time with third-order Adams–Bashforth steps ($\sim 10^3$ steps per background rotation). The Fourier coefficients $\{\Psi^{(m)}\}$ of the stream function are each decomposed into a background contribution (Ψ_b) and a vortex contribution (Ψ_v): $\Psi = \Psi_b + \Psi_v$. The background contribution satisfies the equation

$$\left[\frac{\partial^2}{\partial r^2} + \frac{1}{r} \frac{\partial}{\partial r} - \frac{m^2}{r^2} \right] \cdot \Psi_b^{(m)}(r, t) = Z^{(m)}(r, t),$$

which is solved to second order accuracy in the radial grid-point spacing ($\sim R_w/2000$). For $m \leq \sqrt{e}r_v(t)/l(t)$, the vortex component of Ψ is given by

$$\Psi_v^{(m)}(r, t) = -\frac{\Gamma_v}{4\pi m} \left(\frac{r <}{r >} \right)^m \left[1 - \left(\frac{r >}{R_w} \right)^{2m} \right] e^{-im\theta_v(t)},$$

where $r >$ ($r <$) is the greater (smaller) of r and $r_v(t)$. The number of (excited) Fourier components is made finite in the linear simulation by setting $\Psi_v^{(m)} = 0$ for $m > \sqrt{e}r_v(t)/l(t)$. With this scheme, the vortex never excites wave numbers greater than the maximum value of $\sqrt{e}r_v/l$ over the vortex

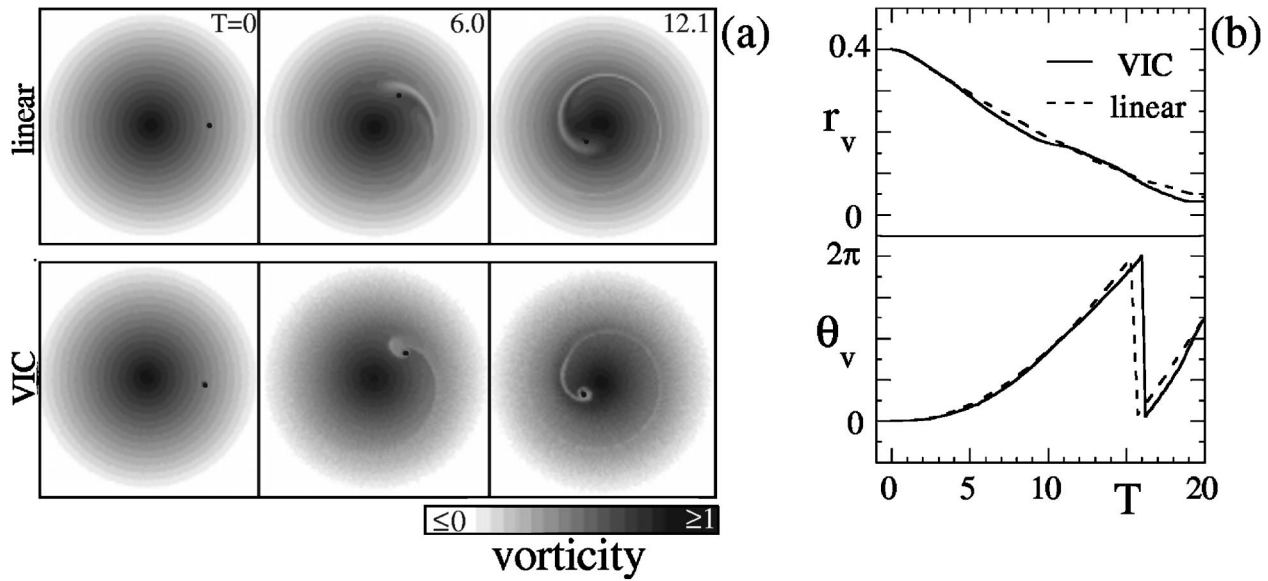


FIG. 7. Inward spiral of a retrograde clump, computed with a linear simulation and a nonlinear VIC simulation: (a) sequence of contour plots, and (b) (r_v, θ_v) vs $T \equiv |\Omega'_o| r_v(0)t$.

trajectory. This cut-off was used (and explained) previously in deriving an analytic expression for the radial velocity of the vortex [Eq. (36)].

We consider the specific case where the initial background vorticity distribution (ζ_b at $t=0$) is given by

$$\zeta_o(r) = \begin{cases} 1 - 1.25 \cdot r, & r \leq 0.8, \\ 0, & r > 0.8. \end{cases} \quad (39)$$

The rotation frequency of this background in the lab frame is $\Omega_o(r) = 0.5 - 0.417 \cdot r$, for $r \leq 0.8$. The background chosen here represents a larger class, where ζ_o decreases monotonically with r , and the radial derivatives ζ'_o and Ω'_o vary slowly with r .

We first examine the motion of clumps, which are *retrograde* in this background. Figure 7 shows the inward spiral of a clump toward the center of the background. The clump strength l/r_v is initially 0.12.

Figure 7(a) shows a sequence of vorticity contour plots for both the linear simulation and the VIC simulation. Although the linear evolution is not identical to the VIC simulation, several features appear similar. These include the rate at which the clump travels toward the center of the distribution, and the wake that is left behind the clump.

Figure 7(b) provides a more concise comparison of the clump trajectories. The top graph shows the linear (dashed line) and the VIC (solid line) computations of $r_v(t)$. There is good agreement between the linear and VIC results. The bottom graph shows that there is similar agreement for $\theta_v(t)$.

It is apparent from Fig. 7(b) that the clump rapidly accelerates to an approximately constant radial speed. In Fig. 8, we plot the value of this speed as a function of the clump strength l/r_v . Here, all clumps start at $r_v = 0.4$ and the background is always given by Eq. (39). The clump strength l/r_v is varied by changing Γ_v only. The value of \dot{r}_v is obtained from a straight-line fit to r_v vs t , as r_v decreases from 0.375 to 0.35. In the plot, \dot{r}_v is normalized to $\zeta'_o r_v^2$. Both $\zeta'_o r_v^2$ and

the clump strength l/r_v are evaluated at $r_v = 0.363$. The diamonds correspond to linear simulations and each ‘‘X’’ corresponds to a VIC simulation. The solid curve is Eq. (38), with $c = 0.43$.

Figure 8 presents several important results. To begin with, the VIC simulations generally agree with the linear simulations. This indicates that the linear equations [Eqs. (25)–(27)] are valid for retrograde vortices, when $l/r_v \ll 1$. Moreover, both simulations are well described by the analytic linear theory of Eq. (38), which relies on the unperturbed orbit approximation and neglects discrete modes of the background. The accuracy of Eq. (38) appears to improve as l/r_v approaches zero.

Good agreement between the simulations and our linear analysis [Eq. (38)] may seem surprising, especially because the analysis neglects the interaction of the vortex with the discrete normal modes of the background (that is, the analysis neglects poles in the Green’s function G). The discrete modes of a cylindrical background flow vary like $e^{i(m\theta - \omega t)}$, and the vortex motion is resonant with a mode if $\dot{\theta}_v = \omega/m$. Using Eq. (27), this resonance condition can also be

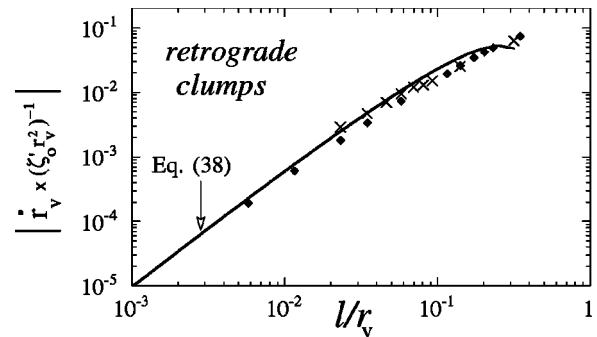


FIG. 8. \dot{r}_v vs l/r_v for retrograde clumps in a linear simulation (diamonds) and a VIC simulation (X’s). The solid line is Eq. (38), with $c = 0.43$.

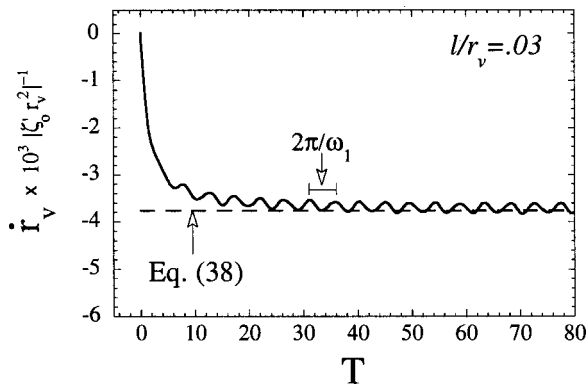


FIG. 9. Radial velocity perturbation that develops at \tilde{r}_v , for a retrograde clump that is artificially fixed on its initial circular orbit. The solid line is a linear simulation, and the dashed line is the time-asymptotic linear theory neglecting discrete modes.

written, $\Omega_o(r_v) = \omega/m$. It has been shown²³ that if the background is monotonic [e.g., Eq. (39)], the latter equation can be satisfied for a discrete mode only if r_v is outside the background vorticity distribution, where ζ'_o is zero. Therefore, a vortex inside the background can not resonate with a discrete mode.

Nevertheless, discrete modes can still exist, and there is a question as to how much they influence the vortex motion. Figure 9 demonstrates explicitly that the effect of the discrete modes is negligible. Here, we plot the radial velocity perturbation that develops at \tilde{r}_v as a function of time, for a vortex that is fixed on its initial circular orbit. The vortex strength is $l/r_v = 0.03$, and the background is given by Eq. (39). To calculate \dot{r}_v , we used the linear simulation, but kept r_v artificially fixed at 0.4.

The value of \dot{r}_v in Fig. 9 rapidly converges to Eq. (38), with $c = 0.43$. Therefore, in deriving Eq. (38), we were justified in neglecting the discrete modes. The only noticeable effect of these modes is small oscillations about the

asymptotic value of \dot{r}_v . These oscillations have the same frequency as the $m = 1$ discrete mode, viewed in a frame that rotates with the orbital angular frequency of the vortex, $\Omega_o(r_v)$. In the lab frame, the frequency ω_1 of the $m = 1$ discrete mode is²⁴ $\Omega_o(R_w)$; therefore, in the rotating frame, $\omega_1 = \Omega_o(R_w) - \Omega_o(r_v)$.

We now consider the motion of prograde holes. Figure 10 shows the outward spiral of a prograde hole toward the edge of the background. As before, the background distribution is given by Eq. (39), and the initial vortex strength l/r_v is 0.12.

Figure 10(a) shows a sequence of contour plots for both the linear simulation and the VIC simulation. In contrast to the motion of a retrograde clump, here there is a dramatic difference between the linear simulation and the VIC simulation: the linear equations give a radial drift that is much too fast. Figure 10(b) shows $r_v(t)$ and $\theta_v(t)$ for both the linear (dashed line) and VIC (solid line) simulations. After $T \sim 1$ there is a sharp divergence between the linear and nonlinear trajectories. This rapid breakdown of linear theory is explained in the next section.

V. NONLINEAR TRAPPING

In this section, we examine the time scale at which linear theory begins to fail in the “mixing layer” that surrounds a vortex in a cylindrical shear-flow. We find that for a prograde vortex, like the hole in Sec. IV, this time scale is practically instantaneous. On the other hand, for a retrograde vortex, the linear time scale becomes infinite as $l/r_v \rightarrow 0$.

Figure 11(a) shows the initial streamlines (in $r - \theta$ space) that are produced by a retrograde vortex in the cylindrical shear flow that is given by Eq. (39). Here, the streamlines are shown in a rotating frame, where the vortex is initially stationary. Figure 11(b) shows the initial streamlines (in $r - \theta$ space) that are produced by a prograde vortex in the same background shear flow. Both flows have mixing layers

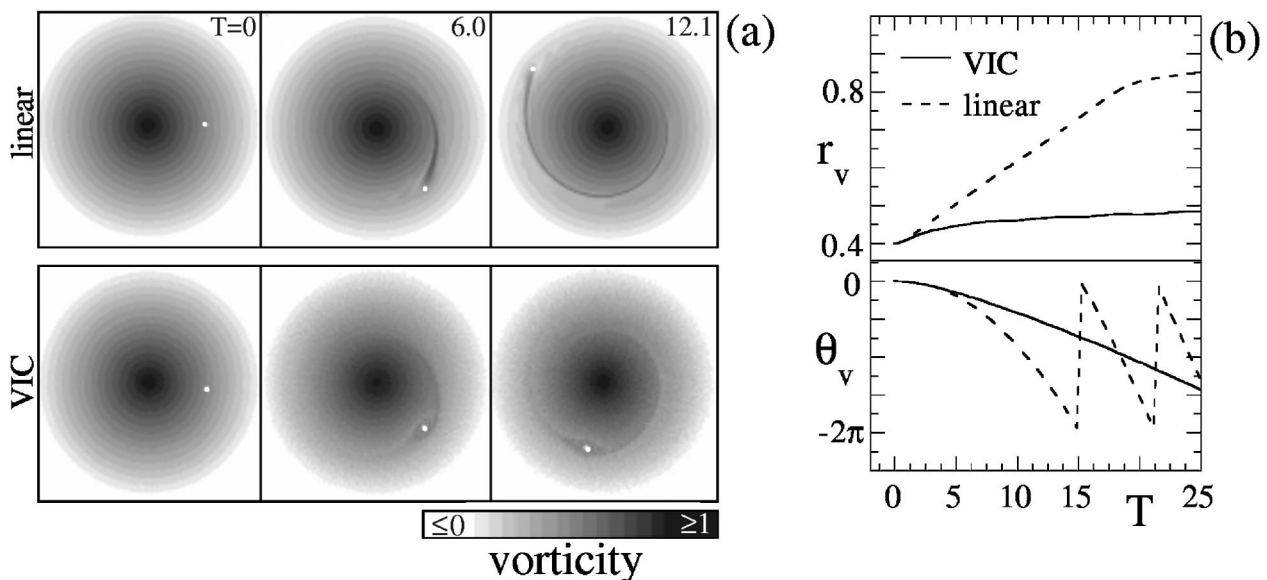


FIG. 10. Outward spiral of a prograde hole, computed with a linear simulation and a nonlinear VIC simulation: (a) sequence of contour plots and (b) (r_v, θ_v) vs $T \equiv |\Omega'_o| r_v(0)t$.

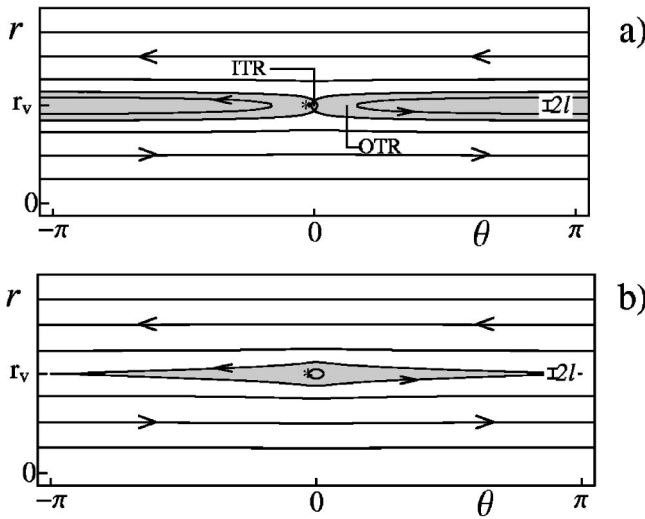


FIG. 11. Initial streamlines and mixing layers (shaded) for (a) a retrograde vortex and (b) a prograde vortex at $r_v=0.4$ in the cylindrical shear-flow that is given by Eq. (39). Both vortices have strength $l/r_v=0.05$. The asterisks correspond to the fluid particles whose orbital periods τ_* give the time scale at which linear theory breaks down.

(shaded) centered at r_v , in which the θ -averaged background vorticity would flatten with time ($d\langle \zeta_b \rangle_\theta / dr \rightarrow 0$), if the vortex remained stationary.

The mixing layer of the retrograde vortex consists of two regions: an inner trapping region (ITR) and an outer trapping region (OTR). This differs from the case of a retrograde vortex in an uncurved shear-flow where there was only one trapping region [shaded region in Fig. 5(a)], corresponding to the ITR. The mixing layer of the prograde vortex consists of only one elongated strip.

The success of linear theory for retrograde vortices and the failure of linear theory for prograde vortices can be understood by considering the streamlines in Fig. 11. In a mixing layer, the fluid particles have secondary orbits, either around the vortex or around a point 180° opposite the vortex. In the jargon of plasma physics, such fluid particles are said to be “trapped” by the vortex. The linearized Euler equation for the evolution of background vorticity [Eq. (23)] does not account for the secondary orbit of a trapped fluid particle, for times greater than or equal to the orbital period.

In developing linear theory, we applied the linearized Euler equation [Eq. (23)] outside a disc of radius $\sim l$, centered at the vortex. This was done indirectly, by imposing the cut-off $m = \sqrt{e} r_v / l$ in Eq. (36). So, we expect linear theory to fail for times greater than the orbital period of a trapped fluid particle initially at \vec{r}_* , where $|\vec{r}_* - \vec{r}_v| \sim l$.

Let τ_* denote the orbital period of a fluid particle that has the initial polar coordinates $(r_v, -2l/r_v)$. This initial position is indicated by a “*” in Fig. 11. The period τ_* is plotted as a function of vortex strength l/r_v in Fig. 12, for both the retrograde case and the prograde case.

For retrograde vortices, the fluid particle is in the OTR, and τ_* diverges to infinity as the vortex strength goes to zero. This divergence occurs because the particle velocity tends to zero (in the rotating frame) with the vortex strength, while the length of the orbit tends to a finite value ($4\pi r_v$).

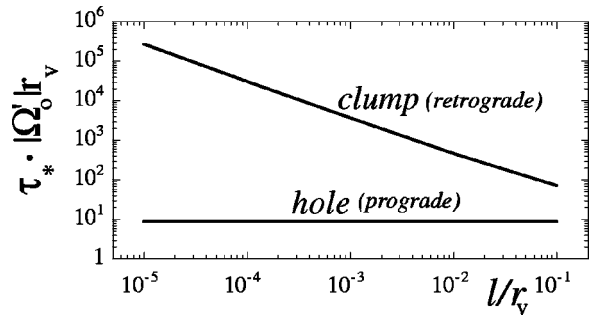


FIG. 12. The time scale (τ_*) at which linear theory breaks down, for prograde and retrograde vortices.

Thus, for retrograde vortices, linear theory stays valid infinitely long as $l/r_v \rightarrow 0$.

For prograde vortices, the fluid particle has an orbit of length $\sim l$ and a velocity that is proportional to l ; therefore τ_* remains constant as $l/r_v \rightarrow 0$. On the other hand, the time scale for the prograde vortex to move a distance of order l becomes infinite. Thus, the time scale for linear theory to fail becomes “instantaneous” relative to the time scale of vortex motion. This explains the sharp contrast between linear theory and the VIC simulation of the trajectory of a prograde hole (Fig. 10).

We emphasize that linear theory fails for the holes in our simulations not because the holes have negative vorticity, but because the holes are prograde with respect to our particular choice of the background shear-flow [Eq. (39)].

VI. MIX-AND-MOVE ESTIMATE FOR PROGRADE VORTICES

In Sec. IV, we showed [Fig. (10)] that linear theory fails to describe the motion of a prograde vortex up/down a background vorticity gradient. In Sec. V, we explained why: a prograde vortex creates a nonlinear perturbation to the background flow “instantaneously.” However, it is still possible to estimate the rate at which a prograde vortex climbs or descends a background vorticity gradient.

In this section, we estimate the radial velocity \dot{r}_v of a prograde vortex in a cylindrical shear-flow, using a “mix-and-move” model of the vortex motion. This model is based on conservation of canonical angular momentum P_θ [Eq. (4)]. A more detailed estimate, which gives the same result, is carried out in Appendix F.

A prograde vortex tends to phase-mix a thin layer of background vorticity, and move a distance Δr in response. This mixing layer (ML) was described in Sec. V, and corresponds to the shaded region in Fig. 11(b). From Fig. 11(b), we see that the ML extends from $\theta = -\pi$ to π and has an average radial width of $\sim 2l$.

Suppose that the prograde vortex levels the entire ML ($d\langle \zeta_b \rangle_\theta / dr \rightarrow 0$) and has a negligible effect on fluid outside the ML. This phase-mixing increases the background component of P_θ by an amount

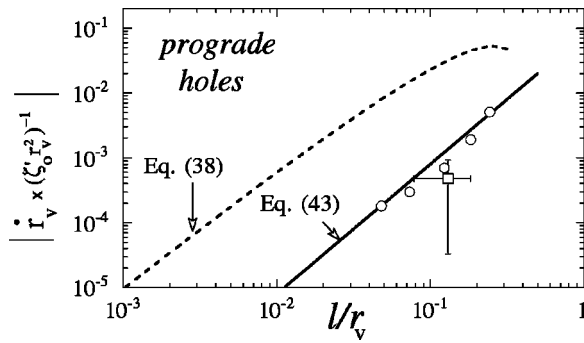


FIG. 13. \dot{r}_v vs l/r_v for prograde holes in a VIC simulation (circles) and an experiment (square). The solid line is the prediction of the “mix-and-move” estimate [Eq. (43)], and the dashed line is the prediction of linear theory [Eq. (38)].

$$\begin{aligned} \Delta P_{\theta,b} &\sim -\zeta'_o \int_{-\pi}^{\pi} d\theta \int_{r_v-l}^{r_v+l} dr r^3 (r-r_v) \\ &= -4\pi \zeta'_o r_v^2 l^3 + O(l^5). \end{aligned} \quad (40)$$

Here, we use the symbol “ \sim ” to indicate that the equation is an estimate. By conservation of P_θ , the radial position r_v of the vortex must change by an amount Δr . Assuming that $\Delta r/r_v \ll 1$, we have

$$\Delta r = \frac{-\Delta P_{\theta,b}}{2\Gamma_v r_v} \sim \pm l \frac{\zeta'_o}{|\Omega'_o|}, \quad (41)$$

where $+/-$ is for clumps/holes.

To obtain the velocity of the prograde vortex also requires an estimate of the time Δt for the ML to flatten. Presumably, this time is given by the orbital period of a fluid particle near the separatrix, which encloses the ML. We estimate that the average angular speed ($\dot{\theta}$) of this fluid particle is $\sim |\Omega'_o|l$, in the frame that rotates with the vortex. Since the orbit covers $\sim 4\pi$ radians (2π in the clockwise direction, and 2π in the counter-clockwise direction), we have

$$\Delta t \sim \frac{4\pi}{|\Omega'_o|l}. \quad (42)$$

Finally, the velocity of the prograde vortex is given by

$$\dot{r}_v \sim \frac{\Delta r}{\Delta t} \sim \pm \frac{1}{4\pi} l^2 \zeta'_o, \quad (43)$$

where $+/-$ is for clumps/holes, and ζ'_o and l are evaluated at the vortex position.

Note that the l -scaling in linear theory [Eq. (38)] differs from the l -scaling in Eq. (43) by a factor of $\ln(cr_v/l)$. Therefore, our estimate suggests that a retrograde vortex, which follows linear theory, will move infinitely faster than a prograde vortex as $l/r_v \rightarrow 0$.

In Fig. 13, we compare Eq. (43) to the late-time prograde hole velocities that are observed in the VIC simulations. As before, ζ'_o is given by Eq. (39) and the prograde holes are located initially at $r_v = 0.4$. The plotted values of \dot{r}_v

are from straight-line fits to r_v vs t , as r_v increases from 0.5 to 0.6. The ratio l/r_v and the velocity normalization $\zeta'_o r_v^2$ are evaluated at $r_v = 0.55$.

The simulation velocities (denoted by O's) are between 0.6 and 1.1 times the values that are predicted by the mix-and-move estimate. Although the estimate is not perfect, it is much more accurate than linear theory (dashed line).

The drift velocity of prograde holes down a vorticity gradient was recently measured by Huang, Fine and Driscoll.² This experiment was performed on a magnetized electron column, which behaves like an ideal 2D fluid. The experiment starts with an unstable flow that rapidly evolves into an axisymmetric vorticity distribution with two (occasionally three) prograde holes (see Ref. 2). Typically these prograde holes are evenly spaced in θ and have roughly the same values for r_v . The remainder of the relaxation is controlled by the slow drift of the prograde holes down the background vorticity gradient, and out of the distribution.

There was some concern that the slow radial drift of prograde holes was a “kitchen effect” of the experiment, which has nothing to do with 2D Euler flow. However, the measured value of \dot{r}_v (plotted in Fig. 13) is within a factor of 3 of Eq. (43), which is at the level of our estimated error. Although strong conclusions should not be drawn from a single datum, it appears that we have captured the fundamental mechanism for the radial motion of prograde holes in the experiments.

A more critical eye might notice, disregarding error bars, that the VIC simulation gives a larger value of \dot{r}_v than the experiment. This suggests that the presence of an additional prograde hole, which changes the structure of the ML, might slow down the outward radial drift. This has been verified by placing an additional prograde hole in the VIC simulation, 180° opposite the original prograde hole (and at the same r_v). The value of \dot{r}_v decreases by a factor of 2, in close agreement with the experiment.

VII. THE SUPPRESSION OF GRADIENT-DRIVEN DRIFT BY LARGE SHEAR

The mix-and-move estimate of the previous section assumes that the prograde vortex continuously moves into new regions where the θ -averaged background vorticity is unperturbed; that is, where $d\langle \zeta_b \rangle_\theta / dr \approx \zeta'_o$. However, if the mixing layer (ML) moves with the prograde vortex, $d\langle \zeta_b \rangle_\theta / dr$ shortly becomes zero at r_v , and the radial drift stops.

We propose that most of the ML moves adiabatically with the prograde vortex, and the radial drift is suppressed, when

$$t_l \gg \Delta t. \quad (44)$$

Here, t_l is the predicted time for r_v to change by l , which is the radial length scale of the ML, and Δt is the time required for the ML to be phase-mixed.

In the previous section, we argued that the mixing time Δt is approximately $4\pi/l|\Omega'_o|$ [Eq. (42)]. The “escape time” t_l is given by $l/|\dot{r}_v|$. Here, we assume that \dot{r}_v is given

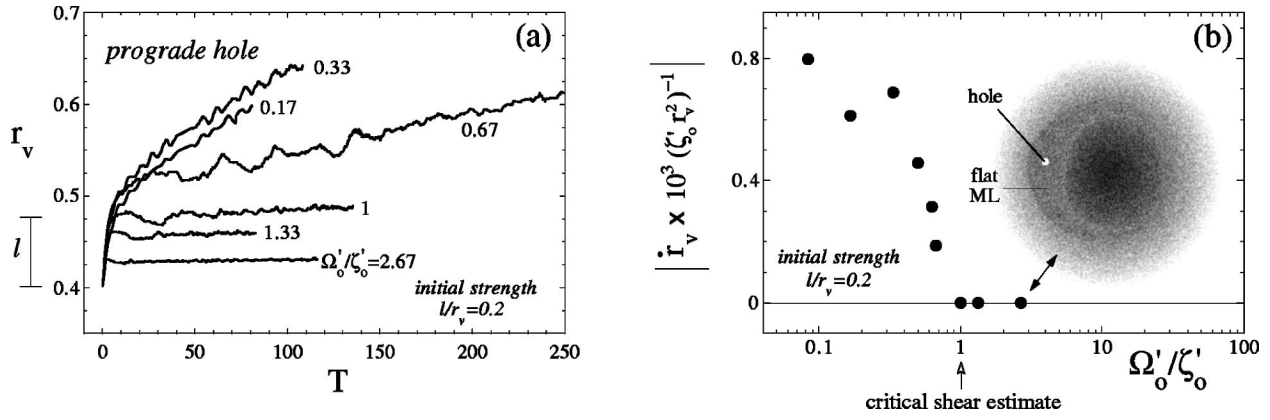


FIG. 14. VIC simulations of the motion of a prograde hole in different levels of background shear. (a) r_v vs T for different shear strengths. (b) \dot{r}_v vs Ω'_o/ζ'_o . Inset: equilibrium obtained for $\Omega'_o/\zeta'_o=2.67$.

by Eq. (43). Putting these estimates into Eq. (44) yields the following condition for no radial drift (past a displacement of order l):

$$\frac{\Omega'_o}{\zeta'_o} \gg 1. \tag{45}$$

Equation (45) indicates that a large shear prevents the prograde vortex from drifting radially.

Alternatively, one can propose that radial drift is suppressed when $l \gg \Delta r$. Here, Δr is the radial displacement of the prograde vortex due to phase-mixing of the entire ML, and is determined by conservation of P_θ . In the previous section, we estimated that $\Delta r \sim l \zeta'_o / \Omega'_o$ [Eq. (41)]. Using this result, we regain Eq. (45) for the suppression of radial drift.

For the simulation data in Fig. 13, $\Omega'_o/\zeta'_o = \frac{1}{3}$, so only a small fraction of the ML moves with the prograde hole.²⁵ However, by artificially increasing $|\Omega'_o|$ in the VIC simulation, so that Ω'_o/ζ'_o has an order of magnitude that is greater than or equal to 1, we can examine the motion of a prograde hole when the mix-and-move model breaks down.

Figure 14 shows how \dot{r}_v changes with Ω'_o/ζ'_o for prograde holes of initial strength $l/r_v=0.2$. The background vorticity is given by Eq. (39); however, the shear Ω'_o is generally not consistent with Poisson's equation. Instead, the fluid particles in the VIC simulation are given an additional angular rotation frequency of the form $S \cdot r$, where the constant S is an adjustable parameter. The initial vortex strength $l/r_v(t=0)$ is kept fixed in this set of simulations by increasing the magnitude of Γ_v in proportion to the total shear Ω'_o .

Figure 14(a) shows r_v as a function of time for different shear strengths. Here, $T \equiv |\Omega'_o| r_v(0) t$, with Ω'_o evaluated for the case of no additional shear ($S=0$). Figure 14(b) shows \dot{r}_v vs Ω'_o/ζ'_o . The value of \dot{r}_v is obtained by a straight line fit to r_v vs. t , as the prograde hole moves from $r_v=0.5$ to 0.6. For $\Omega'_o/\zeta'_o < 1$, \dot{r}_v is approximately constant, and equal to ~ 0.6 times the simple mix-and-move estimate, Eq. (43).²⁶ However, \dot{r}_v drops to zero at $\Omega'_o/\zeta'_o \approx 1$, as predicted by Eq. (45). A velocity of zero means that the hole stops drifting outward before a radial displacement of l .

The inset of Fig. 14(b) is a contour plot of the equilibrium that forms when $\Omega'_o/\zeta'_o=2.67$. Note that the ML has been flattened. The gray levels are the same as in Figs. 7 and 10. We remark that the equilibration observed here is analogous to the nonlinear saturation of a growing (or decaying) plasma wave; i.e., it is akin to the formation of a Bernstein–Greene–Kruskal (BGK) mode.²⁷ A BGK mode forms through the flattening of the electron distribution function in a resonant layer; here, an asymmetric equilibrium forms through the flattening of the θ -averaged vorticity distribution in the mixing layer.

Equation (45) suggests that, for prograde vortices, the shear strength required to suppress outward radial drift does not depend explicitly on l (i.e., on $|\Gamma_v|$). This result is consistent with the VIC simulation data in Fig. 15. Here, the radial velocity is plotted as a function of shear strength Ω'_o/ζ'_o , for initial prograde hole strengths l/r_v that range from 0.08 to 0.4. All cases show the same qualitative behavior. When $\Omega'_o/\zeta'_o \leq 1$, \dot{r}_v is approximately given by the mix-and-move estimate. On the other hand, when $\Omega'_o/\zeta'_o \geq 1$, \dot{r}_v is zero.

A stronger shear is required to suppress the radial drift of a retrograde vortex. The general criterion is presumably the same as for a prograde vortex, $t_l \gg \Delta t$. However, the mixing time Δt and escape time t_l both differ.

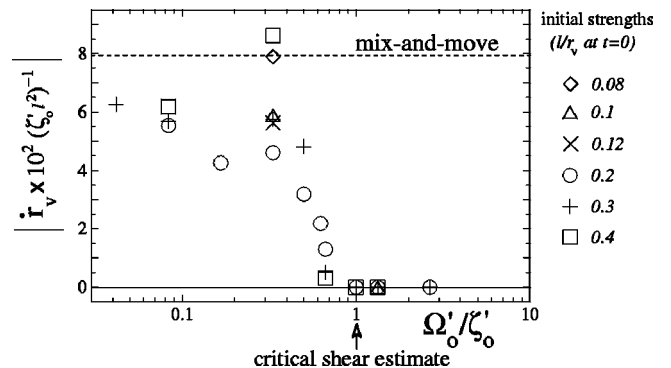


FIG. 15. \dot{r}_v vs Ω'_o/ζ'_o for prograde holes with initial strengths l/r_v that range from 0.08 to 0.4. The critical local shear-rate for the suppression of radial drift seems to be independent of l , as predicted for prograde holes by Eq. (45).

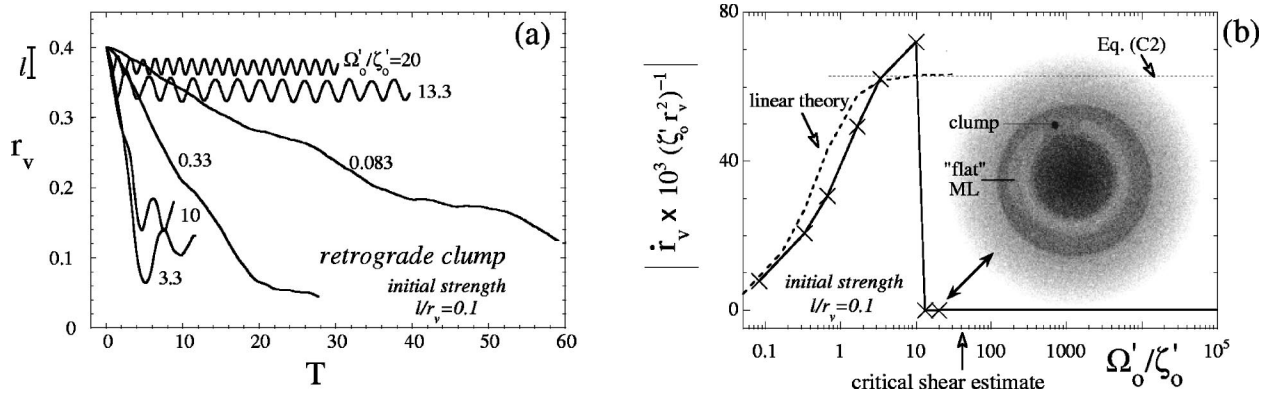


FIG. 16. VIC simulations of the motion of a retrograde clump in different levels of background shear. (a) r_v vs T for different shear strengths. (b) \dot{r}_v vs Ω'_o/ζ'_o . The \times 's are data from VIC simulations. The solid line connects points to aid the eye. The dashed line is Eq. (38), with c a function of Ω'_o . Inset: "equilibrium" obtained for $\Omega'_o/\zeta'_o=20$.

We show in Appendix F that, for a retrograde vortex, $\Delta t \sim 4\sqrt{2}\pi/|\Omega'_o|l\sqrt{\ln(r_v/l)}$. Furthermore, we use the linear theory for \dot{r}_v [Eq. (38), with $c=1$] to estimate the escape time $t_l \equiv l/|\dot{r}_v|$. Then, the condition for an equilibrium to form ($t_l \gg \Delta t$) becomes

$$\frac{\Omega'_o}{\zeta'_o} \gg \sqrt{8\pi^2 \ln(r_v/l)}. \quad (46)$$

Equation (46) is more stringent than Eq. (43) for prograde vortices. According to Eq. (46), as $l/r_v \rightarrow 0$, an infinite shear is required to suppress the radial drift of a retrograde vortex.

Figure 16 illustrates how \dot{r}_v changes with Ω'_o/ζ'_o for retrograde clumps, of initial strength $l/r_v=0.1$. As before, the background vorticity is given by Eq. (39), and the shear is varied artificially. Figure 16(a) shows r_v as a function of time for different shear strengths. Figure 16(b) shows \dot{r}_v as a function of Ω'_o/ζ'_o . The value of \dot{r}_v is obtained from a straight-line fit to r_v vs t , as the retrograde clump moves from $r_v=0.375$ to 0.35 . As Ω'_o/ζ'_o increases, \dot{r}_v increases and then drops to zero at $\Omega'_o/\zeta'_o \sim 10$. This transition point has the same order of magnitude as the critical shear strength estimate, $\sqrt{8\pi^2 \ln(r_v/l)}$, which is indicated on the graph.

The inset of Fig. 16(b) is a contour plot of the "equilibrium" that forms when $\Omega'_o/\zeta'_o=20$. Here, we put "equilibrium" in quotes, because the ML is not fully phase-mixed by the time the simulation was stopped.

It is worth mentioning that linear theory still captures the initial increase in \dot{r}_v with the shear strength. The dashed curve in Fig. 16(b) corresponds to linear theory of \dot{r}_v , Eq. (38). In Fig. 16(b), the shear strength is varied keeping l fixed; so, \dot{r}_v [Eq. (38)] varies with the shear strength only through the variable c in the argument of the logarithm. In Fig. 16(b), it is shown that \dot{r}_v (in linear theory) asymptotes to a fixed value as $\Omega'_o/\zeta'_o \rightarrow \infty$. An analytic expression [Eq. (C2)] for this "infinite" shear limit of \dot{r}_v is derived in Appendix C.

Note that in Fig. 16(b), the curve for linear theory was calculated with $l/r_v=0.116$, which is slightly greater than the initial vortex strength, $l/r_v=0.1$. The larger vortex strength is due to the change in l/r_v from the initial vortex position ($r_v=0.4$) to the point where the radial velocity is measured ($r_v=0.363$).

VIII. DISCUSSION

Two-dimensional vortex motion driven by a background vorticity gradient has been examined numerically and analytically. As illustrated in Figs. 2 and 3, clumps (vorticity excesses) move toward peaks in background vorticity, whereas holes (vorticity deficits) move toward minima.^{3,18} The rate of this migration is determined by whether the vortex is retrograde or prograde [Eq. (5)]: a weak retrograde vortex moves orders of magnitude faster than a prograde vortex of equal strength.

In Sec. II, we presented a simple analytic theory of vortex motion driven by a background vorticity gradient. This theory was based on a reduced linear equation for the evolution of background vorticity [Eq. (12)]. In a few steps, we derived a closed-form expression for the vortex speed [Eq. (16)]. This expression showed that the vortex speed increases with the magnitude of the local background vorticity gradient, and decreases as the local shear intensifies.

In Sec. III, we carried out a more detailed analysis of gradient-driven vortex motion, for the case of a point-vortex in an axisymmetric background. This theory was also based on a linear equation for the evolution of background vorticity [Eq. (23)], but kept various terms that were neglected in Sec. II. Despite the additional terms, we showed that the vortex velocity [Eq. (36)] reduces to the simple result of Sec. II [Eqs. (16) and (38)], as $l/r_v \rightarrow 0$. However, upon comparison to vortex-in-cell simulations, linear theory proved accurate only for retrograde vortices. A prograde vortex always creates a nonlinear perturbation to the background flow, and moves at a much slower rate. Interestingly, a good estimate [Eq. (43)] of this rate was obtained from a simple "mix-and-move" model of the vortex motion.

Of course, the principal results of Secs. III–VI [Eqs. (38) and (43)] have limits of applicability. To begin with, the vortex must be weak compared to the background shear flow; for example, if the shear flow is cylindrical, we require that $l/r_v \ll 1$. Second, the vortex must not resonate with a discrete normal mode (or quasi-mode) of the background (see Sec. IV). In addition, the background shear rate must not exceed a critical level [Eqs. (45) and (46)], beyond which gradient-driven vortex motion is suppressed.

Furthermore, the viscosity of the fluid must be negligible. In particular, we require that the kinematic viscosity ν satisfy the following:

$$\nu \ll l^2/\tau, \tag{47}$$

where τ is the projected time scale of vortex motion through the background. If Eq. (47) is satisfied, then viscosity acts only at length scales $\ll l$, over the time period of interest ($t \lesssim \tau$). In the theory of vortex motion presented here, the structure of the background vorticity perturbation is unimportant at these small scales. However, if $\nu \gtrsim l^2/\tau$, viscosity creates large scale ($\gtrsim l$) changes to the background vorticity, and thereby alters the vortex motion. We note that Eq. (47) is also required to keep a (retrograde) vortex intact. If $\nu \gtrsim l^2/\tau$, then the vortex will diffuse over a separatrix, into a region where the background shear-flow dominates the circular vortex flow. As a result, the vortex will be sheared apart in a time less than or equal to τ .

Our study of gradient-driven vortex motion was in part motivated by an electron plasma experiment on the free relaxation of an unstable cylindrical shear-flow.² In this experiment, the shear-flow developed into a state with multiple vorticity holes in an axisymmetric background. In time, these prograde holes crept radially outward, toward a minimum in the background vorticity distribution. The measured hole velocity proved to be consistent with Eq. (43). Recently, a complementary set of experiments¹³ measured the relaxation rate of a cylindrical shear-flow that contained small-scale vorticity clumps. In these experiments, the retrograde clumps moved to peaks in the background vorticity at a rate consistent with Eq. (38).

We speculate that the results of this article can also serve as a ‘‘zeroth-order’’ model of certain atmospheric flows. For example, Eqs. (38) and (43) may provide reasonable approximations for the motion of small retrograde and prograde vortices (respectively) within a larger tropical cyclone. In addition, Eq. (16) may provide a reasonable estimate for the north-south drift of a retrograde vortex on a planet with strongly sheared (east-west) zonal winds. In this case, the large scale cut-off L , which appears in Eq. (16), is likely the width of a zone.

Of course, a planetary vortex is not governed by 2D Euler flow [Eqs. (1a)–(1c)]. In the ‘‘shallow-water’’ theory of planetary flow, potential vorticity $q \equiv (\zeta + f)/h$ replaces vorticity ζ as the conserved quantity along the Lagrangian trajectory. Here, f is the Coriolis parameter and h is the thickness of the atmosphere. The effect of background potential vorticity (PV) is similar to the effect of background vorticity in 2D Euler flow.^{3–12} So, in a planetary atmosphere, we expect to find long-lived clumps (rotating counter-clockwise) on PV maxima, and long-lived holes (rotating clockwise) on PV minima.

This equilibrium appears to be consistent with the arrangement of long-lived hurricanes in Jupiter’s atmosphere. Figure 17, adapted from Ref. 28, shows the velocity \bar{u} of Jupiter’s east-west zonal winds as a function of latitude. This graph also shows that the long-lived hurricanes rest approximately on zeros of \bar{u} .

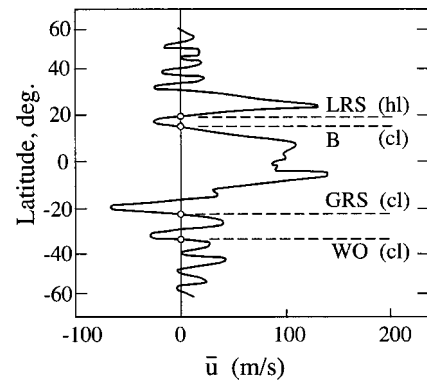


FIG. 17. Location of long-lived storms in Jupiter’s zonal flow (Ref. 28). LRS, B, GRS and WO denote Little Red Spot, Barges, Great Red Spot and White Ovals, respectively. ‘‘cl’’ denotes clump and ‘‘hl’’ denotes hole.

According to Dowling’s model,²⁹ the zonal wind \bar{u} is related to the background potential vorticity \bar{q} on Jupiter by the following: $\bar{u} \approx g \bar{q}_y (\bar{q})^{-2}$. Here, y is the local Cartesian coordinate that increases in the northward direction, g is the (positive) reduced gravity, and \bar{q}_y denotes the derivative of \bar{q} with respect to y . If this model is correct, then Fig. 17 implies that clumps are on potential vorticity peaks ($\bar{q}_y = 0, \bar{q}_{yy} < 0$), whereas holes are in potential vorticity troughs ($\bar{q}_y = 0, \bar{q}_{yy} > 0$).

As a final note, the work presented in this article assumes that a background vorticity gradient already exists. Also, clumps, holes and background were treated as separate entities, whereas in fact all contribute to the overall vorticity. Our results suggest that a preexisting overall vorticity gradient could be amplified as clumps and holes congregate in the peaks and troughs of the background. The motion of clumps and holes through a background vorticity could therefore provide a mechanism for the spontaneous formation of zonal flows. In order to study this transport process, it is necessary to consider the interaction of many clumps and holes and their effect on background vorticity. These subjects will be considered in future work.

ACKNOWLEDGMENTS

The authors gratefully acknowledge useful conversations with Professor T. M. O’Neil, Professor C. F. Driscoll, and Dr. A. Kabantsev.

This work was supported by National Science Foundation Grant No. PHY-9876999 and Office of Naval Research Grant No. N00014-96-1-0239.

APPENDIX A: EVALUATION OF THE u -INTEGRAL

In this appendix, we evaluate the u -integral in Eq. (15), which gives the time dependence of the vortex’s radial velocity \dot{r}_v .

Let $I(t)$ denote the integral:

$$I(t) \equiv \int_{-\infty}^{+\infty} du \frac{u}{u^2 + 1} \ln \left[\frac{u^2 + 1}{(u - At)^2 + 1} \right]. \tag{A1}$$

To evaluate $I(t)$, we first express the fraction $u/(u^2 + 1)$ as a sine transform. Then,

$$\frac{u}{u^2+1} = \int_0^\infty dk e^{-k} \sin(ku). \quad (\text{A2})$$

Substituting Eq. (A2) into Eq. (A1) yields

$$I(t) = \int_0^\infty dk \int_{-\infty}^\infty d\nu \ln \left[\frac{(\nu + At/2)^2 + 1}{(\nu - At/2)^2 + 1} \right] \times e^{-k} \sin(k\nu) \cos\left(k \frac{At}{2}\right). \quad (\text{A3})$$

Here, we have also made the transformation of variables $u \rightarrow \nu$, where $\nu = u - At/2$.

The ν integral in Eq. (A3) is in Ref. 30:

$$\int_{-\infty}^\infty d\nu \ln \left[\frac{(\nu + At/2)^2 + 1}{(\nu - At/2)^2 + 1} \right] \sin(k\nu) = \frac{4\pi}{k} e^{-k} \sin\left(k \frac{At}{2}\right). \quad (\text{A4})$$

Substituting Eq. (A4) into Eq. (A3), we obtain

$$I = 2\pi \int_0^\infty dk e^{-2k} \frac{\sin(kAt)}{k} = 2\pi \tan^{-1}(T/2) \text{sgn}(A), \quad (\text{A5})$$

where $T = |A|t$. Equation (A5) is the desired result.

APPENDIX B: THE GREEN'S FUNCTION

In this appendix we describe how to calculate the Green's function $G(r|r_v, s)$ of the differential operator D_s [Eq. (32)], in the limit that s goes to zero along the positive real axis.

1. General solution

The Green's function is defined by the equation

$$D_s[G(r|r_v, s)] \equiv \left[\frac{\partial^2}{\partial r^2} + \frac{1}{r} \frac{\partial}{\partial r} - \frac{m^2}{r^2} - \frac{im\zeta'_o(r)}{r[s + im\Omega_o(r)]} \right] \cdot G(r|r_v, s) = \frac{\delta(r-r_v)}{r_v}, \quad (\text{B1})$$

and the boundary conditions $G(0|r_v, s) = G(R_w|r_v, s) = 0$. Equation (B1) has the formal solution

$$G(r|r_v, s) = \frac{f_s(r_<)h_s(r_>)}{r_v W_s(r_v)}. \quad (\text{B2})$$

Here, $r_>$ ($r_<$) is the greater (smaller) of r and r_v . The functions $f_s(r)$ and $h_s(r)$ are independent solutions to the homogeneous equation; that is, $D_s[f] = D_s[h] = 0$. They are distinct in that $f_s(r)$ vanishes at $r=0$, whereas $h(r)$ vanishes at R_w . The Wronskian $W_s(r)$ is defined by the equation $W_s(r) = f_s(r)h'_s(r) - h_s(r)f'_s(r)$.

For small m , the functions f_s and h_s are found numerically, using standard methods. To obtain the radial drift of the vortex [Eq. (36)], we need $G(r|r_v, s)$ in the limit that $s \rightarrow 0^+$. Therefore, we decrease s along the positive real axis until the Green's function converges to its limiting form.

2. Analytic solution for large m

We now demonstrate that the imaginary part of $G(r_v|r_v, 0^+)$ is given by Eq. (37) for large m .

For analysis, it is convenient to rewrite the differential equation for the Green's function, Eq. (B1), as follows:

$$\left[L - \frac{im\zeta'_o(r)}{r[s + im\Omega_o(r)]} \right] \cdot G(r|r_v, s) = \frac{\delta(r-r_v)}{r_v}. \quad (\text{B3})$$

Here, L is the Fourier transform of the 2D Laplacian,

$$L \equiv \frac{\partial^2}{\partial r^2} + \frac{1}{r} \frac{\partial}{\partial r} - \frac{m^2}{r^2}. \quad (\text{B4})$$

Note that G in Eq. (B3) has an implicit m -dependence.

We now decompose the Green's function into two parts:

$$G(r|r_v, s) \equiv g_o(r|r_v) + g_1(r|r_v, s). \quad (\text{B5})$$

Here $g_o(r|r')$ is the Green's function of L ,

$$L[g_o(r|r')] = \frac{\delta(r-r')}{r'}, \quad (\text{B6})$$

and accounts for the vortex stream function. The explicit functional form of $g_o(r|r_v)$ is given by the following:

$$g_o(r|r_v) \equiv -\frac{1}{2m} \left(\frac{r_<}{r_>} \right)^m \left[1 - \left(\frac{r_>}{R_w} \right)^{2m} \right], \quad (\text{B7})$$

where $r_>$ ($r_<$) is the greater (smaller) of r and r_v .

The 'correction' g_1 accounts for the response of the background to the vortex. Substituting Eq. (B5) into Eq. (B3) gives the following differential equation for g_1 :

$$L[g_1(r|r_v, s)] = \frac{im\zeta'_o(r)}{r[s + im\Omega_o(r)]} [g_o(r|r_v) + g_1(r|r_v, s)]. \quad (\text{B8})$$

A formal integral solution to Eq. (B8) is as follows:

$$g_1(r|r_v, s) = \int_0^{R_b} dr' g_o(r|r') \frac{im\zeta'_o(r')}{[s + im\Omega_o(r')]} \times [g_o(r'|r_v) + g_1(r'|r_v, s)], \quad (\text{B9})$$

where R_b is the radial extent of the background vorticity distribution. We can use the Plemelj formula (and some minor algebra) to evaluate the integral in the limit $s \rightarrow 0^+$, yielding

$$g_1(r|r_v, 0^+) = P \int_0^{R_b} dr' \frac{\zeta'_o(r')}{\Omega_o(r')} \left[1 + \frac{g_1(r'|r_v, 0^+)}{g_o(r'|r_v)} \right] g_o(r|r') g_o(r'|r_v) + \frac{i\pi\zeta'_o(r_v)}{|\Omega'_o(r_v)|} \left[1 + \frac{g_1(r_v|r_v, 0^+)}{g_o(r_v|r_v)} \right] g_o(r_v|r_v) g_o(r|r_v). \quad (\text{B10})$$

Note that the Plemelj formula applies at $r=r_v$, since $\Omega_o(r_v)=0$ in the rotating frame.

So far, we have made no approximations. However, for large m , we will assume that

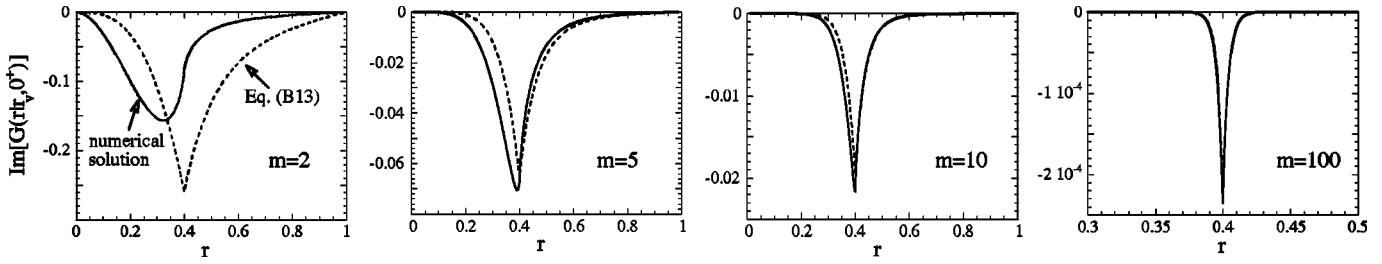


FIG. 18. Convergence of $\text{Im}[G]$ to Eq. (B13) as $m \rightarrow \infty$.

$$|g_1(r|r_v, 0^+)| \ll |g_o(r|r_v)|. \quad (\text{B11})$$

Then, for large m , the terms involving g_1/g_o in Eq. (B10) can be neglected, yielding

$$g_1(r|r_v, 0^+) = P \int_0^{R_b} dr' \frac{\zeta'_o(r')}{\Omega'_o(r')} g_o(r|r') g_o(r'|r_v) + g_o(r|r_v) \frac{i\pi\zeta'_o(r_v)}{|\Omega'_o(r_v)|} g_o(r_v|r_v). \quad (\text{B12})$$

Equation (B12) gives a solution that is consistent with our original assumption, Eq. (B11), in the limit of large m : From Eq. (B7), we have $g_o \sim 1/m$, and by inspection of Eq. (B12), we have $g_1 \sim 1/m^2$. Therefore, $|g_1| \ll |g_o|$ for large m .

We are interested primarily in the imaginary part of $G(r|r_v, 0^+)$, since it alone contributes to \dot{r}_v [Eq. (36)]. Since g_o is real, the imaginary part of $G(r|r_v, 0^+)$ is equal to the imaginary part of $g_1(r|r_v, 0^+)$.

In the large m limit, we argued that $g_1(r|r_v, 0^+)$ is given by Eq. (B12). The integral in Eq. (B12) is real. So, in the large m limit, the imaginary part of $G(r|r_v, 0^+)$ is given solely by the second term on the right-hand side of Eq. (B12); that is,

$$\text{Im}[G(r|r_v, 0^+)] \approx g_o(r|r_v) \frac{\pi\zeta'_o(r_v)}{|\Omega'_o(r_v)|} g_o(r_v|r_v). \quad (\text{B13})$$

Equation (B13) is compared to a numerical solution in Fig. 18. Here, the background is given by Eq. (39), and $r_v = 0.4$. The numerical solution for $\text{Im}[G(r|r_v, 0^+)]$ is in good agreement with Eq. (B13), for $m \geq 10$.

We now use Eq. (B13) to evaluate $\text{Im}[G(r_v|r_v, 0^+)]$, which appears in Eq. (36) for \dot{r}_v . Substituting Eq. (B7) for g_o into Eq. (B13), we find that

$$\text{Im}[G(r_v|r_v, 0^+)] \approx \frac{\pi\zeta'_o(r_v)[1 - (r_v/R_w)^{2m}]^2}{4m^2|\Omega'_o(r_v)|}. \quad (\text{B14})$$

For large m , the quantity $(r_v/R_w)^{2m}$ is negligible, and Eq. (B14) reduces to Eq. (37) of the main text.

APPENDIX C: LINEAR THEORY FOR \dot{r}_v IN THE CASE OF VERY STRONG BACKGROUND SHEAR

In Sec. VII, we discussed the effect of large shear on \dot{r}_v . Our primary point was that large shear brings \dot{r}_v to zero, by causing the mixing layer to flatten rapidly. However, this suppression of radial drift occurs only when Ω'_o/ζ'_o exceeds a critical level [Eqs. (45) and (46)]. For weaker shear, we

found that linear theory provides a good approximation for \dot{r}_v , in the case of a retrograde vortex. Moreover, we saw that in linear theory, \dot{r}_v asymptotes to a finite value as $\Omega'_o \rightarrow \infty$, keeping l , ζ'_o , r_v and R_w fixed [Fig. 16(b)]. We now calculate this “infinite” shear limit of \dot{r}_v .

We first note that Eq. (B12) is valid for all m , as $\Omega'_o \rightarrow \infty$. In this limit, both terms on the right-hand-side of Eq. (B12) tend to zero, for all m . Therefore, for large shear and all m , Eq. (B12) gives a self-consistent solution; that is, $|g_1| \ll |g_o|$.

This means that for all m we can use Eq. (B14), which gives an expression for $\text{Im}[G(r_v|r_v, 0^+)]$ that is based on Eq. (B12). Substituting Eq. (B14) into Eq. (36) for \dot{r}_v , we obtain

$$\lim_{t \rightarrow \infty} \dot{r}_v = \pm \frac{\pi}{2} \zeta'_o(r_v) l^2 \sum_{m=1}^{\sqrt{e}r_v/l} \frac{1}{m} \left[1 - \left(\frac{r_v}{R_w} \right)^{2m} \right]^2. \quad (\text{C1})$$

Note that this expression for \dot{r}_v depends only on l , ζ'_o , r_v and R_w . If these quantities are held fixed as Ω'_o increases, there will be no change in \dot{r}_v .

For small l/r_v , Eq. (C1) has the following approximate form:

$$\lim_{t \rightarrow \infty} \dot{r}_v = \pm \frac{\pi}{2} \zeta'_o(r_v) l^2 \ln(c_* r_v/l), \quad (\text{C2})$$

where c_* is defined as

$$c_* = \lim_{l/r_v \rightarrow 0} \frac{l}{r_v} \exp \left\{ \sum_{m=1}^{\sqrt{e}r_v/l} \frac{1}{m} \left[1 - \left(\frac{r_v}{R_w} \right)^{2m} \right]^2 \right\}. \quad (\text{C3})$$

The dependence of c_* on r_v/R_w was obtained numerically and is plotted in Fig. 19.

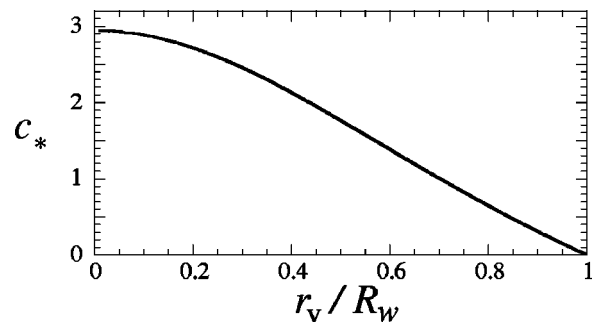


FIG. 19. The “infinite” shear limit of c as a function of r_v/R_w .

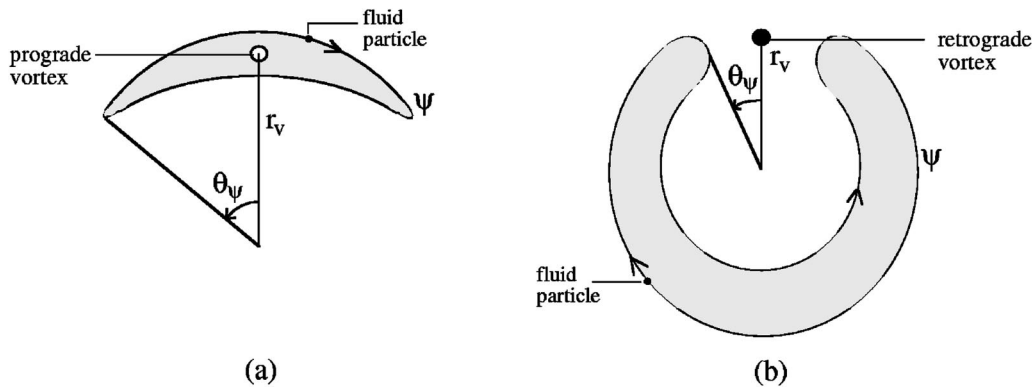


FIG. 20. The streamlines in the mixing layers of a prograde vortex (a) and a retrograde vortex (b) can be parametrized by the angle θ_ψ ($0 \leq \theta_\psi \leq \pi$). This angle is where the streamline passes through r_v .

Figure 16(b) of the main text demonstrates that Eq. (C2) gives the correct value for the ‘infinite’ shear limit of \dot{r}_v , in linear theory.

APPENDIX D: TIME ASYMPTOTIC LIMIT OF THE ω -INTEGRAL

In this appendix, we evaluate the $t \rightarrow \infty$ limit of the ω -integral in Eq. (34), which is required to obtain the late-time limit of \dot{r}_v .

Let $J(t)$ denote this integral:

$$J(t) \equiv \text{P} \int_{-\infty}^{\infty} d\omega \frac{G(r|r_v, 0^+ + i\omega)}{\omega} e^{i\omega t}. \tag{D1}$$

We now make the change of variables $\omega \rightarrow \nu$, where $\nu \equiv \omega t$. In terms of ν , we have

$$J(t) = \text{P} \int_{-\infty}^{\infty} d\nu \frac{G(r|r_v, 0^+ + i\nu/t)}{\nu} e^{i\nu}. \tag{D2}$$

In the $t \rightarrow \infty$ limit, Eq. (D2) becomes

$$\lim_{t \rightarrow \infty} J(t) = G(r|r_v, 0^+) \text{P} \int_{-\infty}^{\infty} d\nu \frac{\cos \nu + i \sin \nu}{\nu}. \tag{D3}$$

The cosine term in Eq. (D3) vanishes, since $\cos \nu/\nu$ is odd. The sine term yields

$$\lim_{t \rightarrow \infty} J(t) = i\pi G(r|r_v, 0^+). \tag{D4}$$

Equation (D4) is the desired result.

APPENDIX E: STREAMLINES IN THE MIXING LAYER

In this appendix, we examine the initial streamlines around a weak vortex in a cylindrical shear-flow. We consider both prograde and retrograde vortices [Eq. (3)]. The results derived here are used in Appendix F to estimate the radial velocity of a prograde vortex, which can not be calculated using linear theory. The results are also used in Appendix F to estimate the critical local shear-rate [Eqs. (45) and (46)] for the suppression of radial drift, for both prograde and retrograde vortices.

Up to an arbitrary constant, the stream function around a vortex of circulation Γ_v in a cylindrical shear-flow $\Omega_o(r)$ is

$$\psi = \int_0^r dr' r' \Omega_o(r') + \frac{\Gamma_v}{4\pi} \ln[r^2 + r_v^2 - 2rr_v \cos(\theta - \theta_v)]. \tag{E1}$$

Here, we have neglected the image of the vortex due to the wall. We now go into a rotating frame where $\Omega_o(r_v)$ is zero, and we set θ_v equal to zero. Furthermore, we assume that Ω'_o is approximately constant. Then, the stream function in Eq. (E1) simplifies to

$$\psi = \Omega'_o \left(\frac{r^3}{3} - \frac{r_v r^2}{2} \right) + \frac{\Gamma_v}{4\pi} \ln(r^2 + r_v^2 - 2rr_v \cos \theta). \tag{E2}$$

The important nonlinear dynamics occurs in the mixing layer (ML). Consequently, we focus on streamlines in this region. We refer the reader to Sec. V, and in particular Fig. 11, for our definition of the ML.

All streamlines are contours along which $\psi(r, \theta)$ is constant. A streamline in the ML is parametrized by the angle θ_ψ ($0 \leq \theta_\psi \leq \pi$), where it passes through r_v (the radial position of the vortex). The angle θ_ψ is defined pictorially in Fig. 20. The separatrix which outlines the ML of a weak ($l/r_v \ll 1$) prograde vortex is the streamline for which $\theta_\psi = \pi$. The separatrix which outlines the ML of a weak retrograde vortex is the streamline for which $\theta_\psi = l/\sqrt{e} r_v$.

The streamline equation is $\psi(r, \theta) = \psi(r_v, \theta_\psi)$, or equivalently

$$\rho^2 + \frac{2}{3} \rho^3 \pm \left(\frac{l}{r_v} \right)^2 \ln \left[\frac{2(1+\rho) \cdot (1 - \cos \theta) + \rho^2}{2(1 - \cos \theta_\psi)} \right] = 0. \tag{E3}$$

Here, $\rho \equiv (r - r_v)/r_v$ and l is defined by Eq. (17). The sign of the third term is ‘+’ for a prograde vortex ($\Gamma_v/\Omega'_o > 0$) and ‘-’ for a retrograde vortex ($\Gamma_v/\Omega'_o < 0$). For $l/r_v \ll 1$, and $\theta \gg l/r_v$, we obtain the following approximation for ρ :

$$\rho(\theta) \approx \begin{cases} \pm \frac{l}{r_v} \sqrt{\ln \left[\frac{1 - \cos \theta_\psi}{1 - \cos \theta} \right]} & \text{prograde} \\ \pm \frac{l}{r_v} \sqrt{\ln \left[\frac{1 - \cos \theta}{1 - \cos \theta_\psi} \right]} & \text{retrograde.} \end{cases} \tag{E4a, E4b}$$

Here, \pm indicates that ρ has a positive and a negative value for any given θ .

APPENDIX F: ANALYSIS OF NONLINEAR MOTION

1. Detailed mix-and-move estimate for \dot{r}_v

We now carry out a detailed mix-and-move estimate for the radial velocity \dot{r}_v of a prograde vortex in an initially axisymmetric background. This detailed estimate yields the same expression for \dot{r}_v as our simple estimate, Eq. (43).

As in the main text, we assume that the prograde vortex acts to level the (coarse-grained) vorticity distribution in the ML [the shaded region in Fig. 11(b)], but has a negligible effect on fluid outside the ML. Then, a reasonable estimate for \dot{r}_v is given by

$$\dot{r}_v \sim \left\langle \frac{-\Delta P_{\theta,b}}{2\Gamma_v r_v \tau} \right\rangle_{\psi}. \quad (\text{F1})$$

Here, $\Delta P_{\theta,b}$ is the change in the background's angular momentum that occurs upon flattening the vorticity distribution in the area between the vortex and a closed streamline [e.g., the shaded region in Fig. 20(a)], τ is the orbital period of a fluid particle on that streamline, and $\langle \rangle_{\psi}$ denotes an average over the streamlines in the ML. We have used conservation of P_{θ} [Eq. (4)] to relate the change in r_v to the change in $P_{\theta,b}$. Note that the orbital period τ is infinite on the separatrix bounding the ML. Therefore, if we used the particle orbit on the separatrix to evaluate \dot{r}_v , instead of an average, we would obtain $\dot{r}_v = 0$.

After the background vorticity is phase-mixed within a closed streamline [shaded area in Fig. 20(a)], it has a constant coarse-grained value ζ_{ψ} in that region. The phase-mixing process that brings $\zeta_o(r)$ to ζ_{ψ} conserves the integral of coarse-grained vorticity in the area bounded by the closed streamline; that is,

$$r_v^2 \int_{-\theta_{\psi}}^{\theta_{\psi}} d\theta \int_{\rho_-(\theta)}^{\rho_+(\theta)} d\bar{\rho} (1 + \bar{\rho}) \cdot [\zeta_{\psi} - \zeta_o(r)] = 0. \quad (\text{F2})$$

Here, $\bar{\rho} \equiv (r - r_v)/r_v$, and ρ_+ (ρ_-) is the positive (negative) branch of $\rho(\theta)$ defined by Eq. (E4a). The angle θ_{ψ} is the maximum angle reached by a fluid particle on the closed streamline [see Fig. 20(a)]. For the separatrix, which bounds the ML, $\theta_{\psi} = \pi$. As we approach streamlines closer to the vortex, θ_{ψ} goes to zero.

The change in $P_{\theta,b}$ that occurs due to phase-mixing within a closed streamline is given by the following integral:

$$\Delta P_{\theta,b}(\theta_{\psi}) = r_v^4 \int_{-\theta_{\psi}}^{\theta_{\psi}} d\theta \int_{\rho_-(\theta)}^{\rho_+(\theta)} d\bar{\rho} (1 + \bar{\rho})^3 [\zeta_{\psi} - \zeta_o(r)]. \quad (\text{F3})$$

To evaluate Eq. (F3), we use Eq. (E4a) for ρ_{\pm} , Eq. (F2) for ζ_{ψ} , and $\zeta_o(r) \approx \zeta_o(r_v) + \zeta_o'(r_v) \cdot (r - r_v)$. Then, to lowest order in l we obtain

$$\Delta P_{\theta,b}(\theta_{\psi}) = -\frac{4}{3} \zeta_o' r_v^2 l^3 \int_{-\theta_{\psi}}^{\theta_{\psi}} d\theta \ln^{3/2} \left[\frac{1 - \cos \theta_{\psi}}{1 - \cos \theta} \right], \quad (\text{F4})$$

where ζ_o' is the short-hand for $\zeta_o'(r_v)$, as usual. Figure 21 shows $\Delta P_{\theta,b}$ [Eq. (F4)] as a function of θ_{ψ} . Here, we see

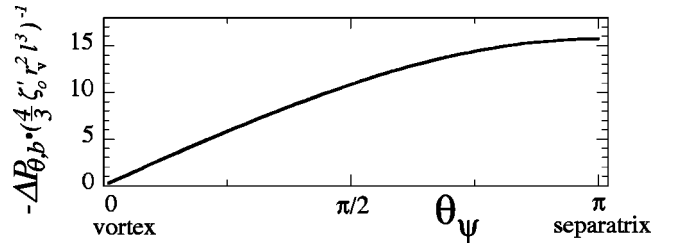


FIG. 21. $\Delta P_{\theta,b}$ vs θ_{ψ} . Here, $\Delta P_{\theta,b}$ is the canonical angular momentum that is transferred to the background flow by a prograde vortex, through phase-mixing of vorticity in the shaded region of Fig. 20(a).

that $\Delta P_{\theta,b}$ increases monotonically with θ_{ψ} , due to the fact that the area in which the vorticity is phase-mixed increases with θ_{ψ} .

The orbital period of a fluid particle is given by

$$\tau(\theta_{\psi}) = 4 \int_{-\theta_{\psi}}^0 d\theta / \dot{\theta}. \quad (\text{F5})$$

Here, $\dot{\theta}$ is the angular velocity of the fluid particle along the streamline. This angular velocity has contributions from the background shear-flow and the vortex field, and can be written as follows:

$$\dot{\theta} = \Omega_o' r_v \cdot \left[\rho + \left(\frac{l}{r_v} \right)^2 \frac{1}{1 + \rho} \cdot \frac{1 + \rho - \cos \theta}{2(1 + \rho)(1 - \cos \theta) + \rho^2} \right]. \quad (\text{F6})$$

For the most part, ρ is $O(l/r_v)$ [see Eq. (E4)]; therefore, it is a reasonable approximation to drop the second term in Eq. (F6). Then, using Eq. (E4a) for ρ , we have

$$\dot{\theta} = \pm \Omega_o' l \sqrt{\ln \left[\frac{1 - \cos \theta_{\psi}}{1 - \cos \theta} \right]}, \quad (\text{F7})$$

where $+$ is for $\rho > 0$ and $-$ is for $\rho < 0$. The expression for τ becomes

$$\tau(\theta_{\psi}) = \frac{4}{|\Omega_o' l|} \int_{-\theta_{\psi}}^0 d\theta \ln^{-1/2} \left[\frac{1 - \cos \theta_{\psi}}{1 - \cos \theta} \right]. \quad (\text{F8})$$

Figure 22 shows τ [Eq. (F8)] as a function of θ_{ψ} . Note that τ becomes infinite near the separatrix ($\theta_{\psi} = \pi$).

Substituting Eqs. (F4) and (F8) into Eq. (F1), we obtain the following expression for \dot{r}_v :

$$\dot{r}_v \sim \pm \frac{1}{4\pi} l^2 \zeta_o' \langle h(\theta_{\psi}) \rangle_{\psi}, \quad (\text{F9})$$

where $+/-$ is for clumps/holes, and the function $h(\theta_{\psi})$ is defined as

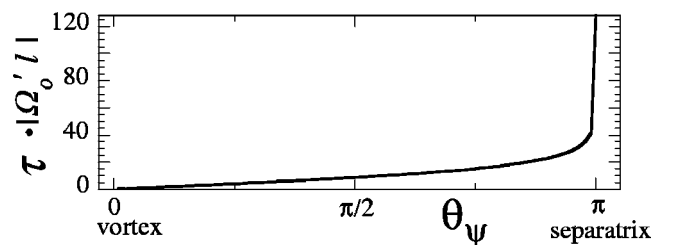


FIG. 22. Orbital period τ vs θ_{ψ} , for a fluid particle encircling a prograde vortex.

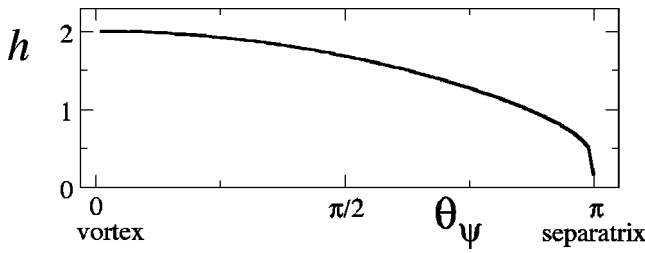


FIG. 23. The function h , appearing in Eq. (F9) for the radial velocity of a prograde vortex.

$$h(\theta_\psi) \equiv \frac{1}{3} \frac{\int_{-\theta_\psi}^{\theta_\psi} d\theta \ln^{3/2}[(1 - \cos \theta_\psi)/(1 - \cos \theta)]}{\int_{-\theta_\psi}^{\theta_\psi} d\theta \ln^{-1/2}[(1 - \cos \theta_\psi)(1 - \cos \theta)]}. \quad (\text{F10})$$

The function $h(\theta_\psi)$ is plotted in Fig. 23. The values of h range from 0 to 2. Moreover, h is of order unity everywhere except in a thin layer near the separatrix ($\theta_\psi = \pi$). Therefore, it is reasonable to choose an averaging scheme such that $\langle h \rangle_\psi = 1$. Then, Eq. (F9) is equivalent to our simple estimate, Eq. (43).

2. Mixing times

We now estimate the time Δt for a vortex to level the surrounding mixing layer (ML). This time was used in Sec. VII to estimate the critical local shear-rate for the suppression of radial drift. Recall that radial drift is suppressed when $\Delta t \ll t_l \equiv l/|\dot{r}_v|$.

We first determine the mixing time for the ML that surrounds a prograde vortex [Fig. 11(b)]. This mixing time Δt_p corresponds to a typical orbital period of a fluid particle in the ML. These orbital periods are shown as a function of θ_ψ in Fig. 22. Unfortunately, the orbital periods range from zero to infinity, so that a ‘‘typical’’ value is not obvious.

However, a better definition for Δt_p is the time for most of the vorticity in the ML to be phase-mixed. Of course, the entire ML takes infinitely long to mix, since the orbital period on the separatrix ($\theta_\psi = \pi$) is infinite. So, rather than set Δt_p equal to $\tau(\pi)$, we set it equal to $\tau(\pi/2)$. That is,

$$\Delta t_p \equiv \tau(\pi/2) = \frac{4}{|\Omega'_o|l} \int_{-\pi/2}^0 d\theta \ln^{-1/2} \left[\frac{1}{1 - \cos \theta} \right]. \quad (\text{F11})$$

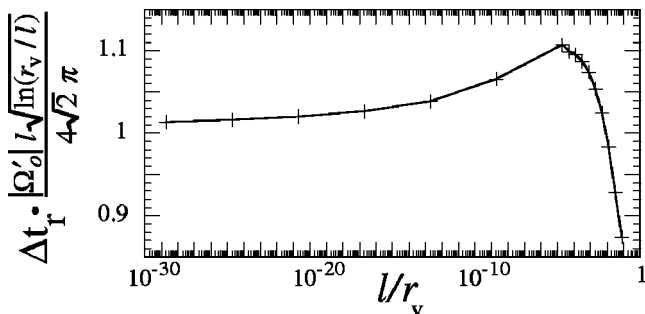


FIG. 24. The mixing time for the retrograde case.

Here we have used Eq. (F8) for the orbital period τ . Note that there is nothing special about $\theta_\psi = \pi/2$, besides the fact that it is $O(1)$.

In Sec. VII, we gave a rough estimate for the mixing time of a prograde vortex:

$$\Delta t_p \sim 4\pi/|\Omega'_o|l. \quad (\text{F12})$$

Equation (F11) gives a value of Δt_p that, for all l/r_v , is 0.68 times this rough estimate.

We now calculate the mixing time Δt_r for the ML that surrounds a retrograde vortex [Fig. 11(a)]. As for the prograde case, we require that most of the vorticity in the ML is phase-mixed by the time Δt_r . Therefore, we will estimate that Δt_r is the orbital period τ of a fluid particle, whose radial position at $\theta = \pi$ is midway between r_v and the separatrix. A straightforward calculation shows that the orbit of this particle intersects r_v at

$$\theta_\psi = \alpha \left(\frac{l}{r_v} \right)^{1/4}, \quad (\text{F13})$$

where $\alpha \equiv 4^{3/8} e^{-1/8}$.

In analogy to Eq. (F8), which gives τ for particles orbiting a prograde vortex, the following equation gives τ for particles in the ML that surrounds a retrograde vortex:

$$\tau(\theta_\psi) = \frac{4}{|\Omega'_o|l} \int_{-\pi}^{-\theta_\psi} d\theta \ln^{-1/2} \left[\frac{1 - \cos \theta}{1 - \cos \theta_\psi} \right]. \quad (\text{F14})$$

Using Eq. (F13) for θ_ψ gives the mixing time Δt_r :

$$\begin{aligned} \Delta t_r &\equiv \tau(\alpha(l/r_v)^{1/4}) \\ &= \frac{4}{|\Omega'_o|l} \int_{-\pi}^{-\alpha(l/r_v)^{1/4}} d\theta \ln^{-1/2} \left[\left(\frac{r_v}{l} \right)^{1/2} \frac{2}{\alpha^2} (1 - \cos \theta) \right]. \end{aligned} \quad (\text{F15})$$

Here, we have used $\cos \theta_\psi \approx 1 - \theta_\psi^2/2$. Note that in contrast to the prograde case [Eq. (F11)], the integral in Eq. (F15) depends on l .

In Sec. VII, we gave the following estimate for the mixing time:

$$\Delta t_r \sim \frac{4\sqrt{2}\pi}{|\Omega'_o|l\sqrt{\ln(r_v/l)}}. \quad (\text{F16})$$

By inspection, one can see that the right-hand side of Eq. (F15) converges to the right-hand side of Eq. (F16), as $l/r_v \rightarrow 0$. Figure 24 shows the rate of this convergence, obtained from a numerical solution to the integral in Eq. (F15).

¹D. A. Schecter and D. H. E. Dubin, ‘‘Vortex motion driven by a background vorticity gradient,’’ *Phys. Rev. Lett.* **83**, 2191 (1999).
²X. P. Huang, K. S. Fine, and C. F. Driscoll, ‘‘Coherent vorticity holes from 2D turbulence decaying in a background shear-flow,’’ *Phys. Rev. Lett.* **74**, 4424 (1995).
³C. G. Rossby, ‘‘On the displacements and intensity changes of atmospheric vortices,’’ *J. Mar. Res.* **7**, 175 (1948).
⁴M. DeMaria, ‘‘Tropical cyclone motion in a nondivergent barotropic model,’’ *Mon. Weather Rev.* **113**, 1199 (1985).

- ⁵J. L. Evans, G. J. Hollan, and R. L. Elsberry, "Interactions between a barotropic vortex and an idealized subtropical ridge. Part I: Vortex motion," *J. Atmos. Sci.* **48**, 301 (1991).
- ⁶G. M. Reznik, "Dynamics of singular vortices on the beta-plane," *J. Fluid Mech.* **240**, 405 (1992).
- ⁷R. K. Smith, "On the theory of tropical cyclone motion," in *Tropical Cyclone Disasters*, edited by J. Lighthill, Z. Zheming, G. J. Holland, and K. A. Emanuel (Peking University Press, Beijing, 1993), p. 264.
- ⁸R. K. Smith and W. Ulrich, "Vortex motion in relation to the absolute vorticity gradient of the vortex environment," *Q. J. R. Meteorol. Soc.* **119**, 207 (1993).
- ⁹G. G. Sutyryn and G. R. Flierl, "Intense vortex motion on the beta plane: Development of beta gyres," *J. Atmos. Sci.* **51**, 773 (1994).
- ¹⁰R. T. Williams and J. C.-L. Chan, "Numerical studies of the beta effect in tropical cyclone motion. Part II: Zonal mean flow effects," *J. Atmos. Sci.* **51**, 1065 (1994).
- ¹¹S. G. Llewellyn Smith, "The motion of a non-isolated vortex on the beta-plane," *J. Fluid Mech.* **346**, 149 (1997).
- ¹²G. F. Carnevale, R. C. Kloosterziel, and G. J. F. Van Heist, "Propagation of barotropic vortices over topography in a rotating tank," *J. Fluid Mech.* **233**, 119 (1991).
- ¹³Y. Kiwamoto, A. Mohri, K. Ito, A. Sanpei, T. Yuyama, and T. Michishita, "2D interaction of discrete electron vortices," *Non-Neutral Plasma Physics III* (American Institute of Physics, Woodbury, NY, 1999); Y. Kiwamoto, K. Ito, A. Sanpei, and A. Mohri, "Dynamics of electron-plasma vortex in background vorticity distribution," *Phys. Rev. Lett.* **85**, 3173 (2000).
- ¹⁴K. S. Fine, A. C. Cass, W. G. Flynn, and C. F. Driscoll, "Relaxation of 2D turbulence to vortex crystals," *Phys. Rev. Lett.* **75**, 3277 (1995).
- ¹⁵D. A. Schechter, D. H. E. Dubin, K. S. Fine, and C. F. Driscoll, "Vortex crystals from 2D Euler flow: Experiment and simulation," *Phys. Fluids* **11**, 905 (1999).
- ¹⁶R. Beebe, "Characteristic zonal winds and long-lived vortices in atmospheres of the outer planets," *Chaos* **4**, 113 (1994); for data.
- ¹⁷G. K. Batchelor, *An Introduction to Fluid Dynamics* (Cambridge University Press, Cambridge, 1967), pp. 528–529.
- ¹⁸C. H. Liu and L. Ting, "Interaction of decaying trailing vortices in spanwise shear-flow," *Comput. Fluids* **15**, 77 (1987).
- ¹⁹T. H. Dupree, "Growth of phase-space density holes," *Phys. Fluids* **26**, 2460 (1983).
- ²⁰N. A. Krall and A. W. Trivelpiece, *Principles of Plasma Physics* (San Francisco Press, San Francisco, 1986).
- ²¹I. M. Lansky, T. M. O'Neil, and D. A. Schechter, "A theory of vortex merger," *Phys. Rev. Lett.* **79**, 1479 (1997).
- ²²The VIC simulation is the same as that used in Ref. 15. Here, we use at most 1025×1025 grid points and 3×10^6 particles. In addition, negative particles are used when necessary to create deep vorticity holes.
- ²³R. J. Briggs, J. D. Daugherty, and R. H. Levy, "Role of Landau damping in crossed-field electron beams and inviscid shear-flow," *Phys. Fluids* **13**, 421 (1970).
- ²⁴R. H. Levy, "Two new results in cylindrical diocotron theory," *Phys. Fluids* **11**, 920 (1968).
- ²⁵In the electron plasma experiment, $\Omega_e'/\zeta_e' \sim 1/7 - 1/2$.
- ²⁶To obtain the mix-and-move estimate, one must evaluate l at $r_v = 0.55$, not at the initial radial position, $r_v = 0.4$. At $r_v = 0.55$, the vortex strength l/r_v is 0.12, as opposed to the initial strength of 0.2.
- ²⁷I. B. Bernstein, J. M. Greene, and M. D. Kruskal, *Phys. Rev.* **108**, 546 (1957); T. M. O'Neil, "Collisionless damping of nonlinear plasma oscillations," *Phys. Fluids* **8**, 2255 (1965).
- ²⁸M. K. Nezhlin, "Rossby solitary vortices, on giant planets and in the laboratory," *Chaos* **4**, 187 (1994).
- ²⁹T. E. Dowling, "A relationship between potential vorticity and zonal wind on Jupiter," *J. Atmos. Sci.* **50**, 14 (1993).
- ³⁰I. S. Gradshteyn and I. M. Ryzhik, *Table of Integrals, Series and Products*, 5th ed., edited by A. Jeffrey (Academic, New York, 1994), p. 613.